

Calibrated Predictive Distributions via Diagnostics for Conditional Coverage

Biprateep Dey^{1†} David Zhao^{2†} Jeffrey A. Newman¹ Brett H. Andrews¹ Rafael Izbicki³ Ann B. Lee²

¹Dept. of Physics and Astronomy and PITT-PACC, University of Pittsburgh, Pittsburgh, PA 15260

²Department of Statistics & Data Science, Carnegie Mellon University, Pittsburgh, PA 15213

³Department of Statistics, Federal University of São Carlos, São Carlos, Brazil

Abstract

Uncertainty quantification is crucial for assessing the predictive ability of AI algorithms. A large body of work (including normalizing flows and Bayesian neural networks) has been devoted to describing the entire predictive distribution (PD) of a target variable Y given input features \mathbf{X} . However, off-the-shelf PDs are usually far from being conditionally calibrated; i.e., the probability of occurrence of an event given input \mathbf{X} can be significantly different from the predicted probability. Most current research on predictive inference (such as conformal prediction) concerns constructing calibrated prediction sets only. It is often believed that the problem of obtaining and assessing entire conditionally calibrated PDs is too challenging. In this work, we show that recalibration, as well as diagnostics of entire PDs, are indeed attainable goals in practice. Our proposed method relies on the idea of regressing probability integral transform (PIT) scores against \mathbf{X} . This regression gives full diagnostics of conditional coverage across the entire feature space and can be used to recalibrate misspecified PDs. We benchmark our corrected prediction bands against oracle bands and state-of-the-art predictive inference algorithms for synthetic data, including settings with a distributional shift. Finally, we produce calibrated PDs for two applications: (i) probabilistic nowcasting based on sequences of satellite images, and (ii) estimation of galaxy distances based on imaging data (photometric redshifts).

1 Introduction

The term Uncertainty Quantification (UQ) is often used for all approaches that go beyond using point estimation of a variable of interest to assess the predictive accuracy of models [Berger and Smith, 2019, Abdar et al., 2021]. In scientific applications, UQ is sometimes more important than point predictions cf., e.g., Gneiting and Katzfuss [2014], Chen et al. [2022]. In engineering and finance, UQ can also be essential for decision-making, like for optimizing supply chains for actual demand [Farmer, 2017, Göttlich and Knapp, 2020]. In this work, we consider the problem of assessing the uncertainty about a continuous response or “target” variable $Y \in \mathbb{R}$ given input features or covariates $\mathbf{X} \in \mathcal{X}$. UQ approaches that yield prediction regions for Y include: *quantile regression* [Koenker and Bassett Jr., 1978, Koenker and Hallock, 2001], which estimates conditional quantile functions $F^{-1}(\alpha|\mathbf{x})$ of Y at specified levels $\alpha \in (0, 1)$, and *conformal prediction* [Vovk et al., 2005, Lei and Wasserman, 2014], which provides a distribution-free approach to constructing prediction regions based upon remapping a measure of conformity between observed and fitted values of Y to quantiles.

Prediction bands are useful in quantifying uncertainties, but we are now witnessing a transformation across scientific disciplines from point forecasts to the **entire predictive distribution (PD)** of Y given \mathbf{x} ; see, e.g., Gneiting [2008] for probabilistic forecasting in weather predictions, Timmermann [2000] for financial risk management, Alkema et al. [2007] for epidemiological projections and Mandelbaum et al. [2008], Malz and Hogg [2022] for the importance of PDs for astrophysical studies.

Common approaches to obtaining PDs include: *conditional density estimation* (CDE), which directly estimates the conditional density functions $f(y|\mathbf{x})$, via, e.g., mixture density networks (MDN; Bishop 1994), kernel mixture networks [Ambrogioni et al., 2017], Bayesian neural networks (see e.g. Goan and Fookes 2020 and references therein), normalizing flows (including neural autoregressive models) [Papamakarios et al., 2019, Kobyzev et al., 2021], Gaussian pro-

[†]equal contribution.
Preprint. Under review.

cess CDEs [Dutordoir et al., 2018], or simpler nonparametric CDE methods [Izbicki and Lee, 2016, 2017, Dalmaso et al., 2020]; *implicit CDE* methods that encode the PD implicitly (e.g., conditional generative adversarial networks or cGANs; [Mirza and Osindero, 2014]); and *quantile regression* methods that estimate all quantiles simultaneously [Chung et al., 2021a, Fasiolo et al., 2021, Tagasovska and Lopez-Paz, 2019, Amerise, 2018, Liu and Wu, 2011].

Though there are many ways one can describe PDs, the models are only useful in practice if they are approximately *individually or conditionally calibrated*, meaning that the estimated cumulative distribution function (CDF) $\hat{F}(y|\mathbf{x}) \approx F(y|\mathbf{x})$ for all $y \in \mathbb{R}$ at every $\mathbf{x} \in \mathcal{X}$. In words, the predicted conditional probability of an event happening given input \mathbf{x} should match its observed probability. Instance-wise uncertainties are crucial in practical applications. For example, weather forecasts may predict the probability of rainfall given the current state of environmental predictors. Similarly, medical research may estimate the efficacy of a drug for individuals of specific demographics after taking a given dose. Achieving instance-wise uncertainties can be important for algorithmic fairness so as not to over- or under-predict risks for certain groups of individuals [Kleinberg et al., 2016, Zhao et al., 2020].

From PDs, one can also derive various quantities of interest, such as moments, kurtosis, prediction intervals, or even more general prediction bands; such as Highest Predictive Density (HPD) regions. By construction, individually calibrated PDs lead to conditionally valid prediction bands. Indeed, if $C_\alpha(\mathbf{X})$ is a prediction band derived from \hat{F} with nominal coverage $1 - \alpha$, individually calibrated prediction distributions \hat{F} imply

$$\mathbb{P}(Y \in C_\alpha(\mathbf{X}) | \mathbf{X} = \mathbf{x}) = 1 - \alpha, \forall \mathbf{x} \in \mathcal{X}. \quad (1)$$

However, off-the-shelf PDs, such as the ones listed above, are usually far from being calibrated: CDEs are typically fitted by minimizing a loss function (e.g, the KL divergence or integral probability metrics [Papamakarios et al., 2019, Dalmaso et al., 2020]) that do not directly depend upon calibration. An additional obstacle to achieving individual calibration is that most metrics that assess the calibration of PDs, such as the probability integral transform (PIT; [Gan and Koehler, 1990]), only assess average or marginal calibration over the entire distribution of $\mathbf{X} \in \mathcal{X}$. Average calibration is often simply referred to as just “calibration” [Naeini et al., 2015, Guo et al., 2017], although it is a well-known problem that one can achieve marginally calibrated distributions, $\mathbb{E}_{\mathbf{X} \sim F_X} [\hat{F}(y|\mathbf{x})] = \mathbb{E}_{\mathbf{X} \sim F_X} [F(y|\mathbf{x})]$, which completely ignore the input \mathbf{x} . For instance, the PIT statistic may be uniformly distributed, even if $\hat{f}(y|\mathbf{x}) = f(y)$ [Schmidt et al., 2020]. More generally, inconsistencies in various regions of the feature space can cancel out to produce optimal results when looked at as an ensemble [Zhao et al., 2021, Jitkrittum et al., 2020a, Luo et al., 2021].

Objectives and Our Approach: We propose a nonparametric and easily interpretable framework for constructing and assessing entire PDs (rather than just prediction sets), which reliably quantifies individual uncertainties (providing individual a.k.a. conditional calibration).

Our approach builds on the key observation that an estimate \hat{F} is conditionally calibrated if and only if its probability integral transform (PIT) value $\text{PIT}(Y; \mathbf{X}) := \hat{F}(Y|\mathbf{X})$ is uniformly distributed *conditionally on* \mathbf{x} . Thus, if a model is well-calibrated, $r^{\hat{F}}(\gamma; \mathbf{x}) := \mathbb{P}(\text{PIT}(Y; \mathbf{X}) \leq \gamma | \mathbf{x})$ is close to γ for all \mathbf{x} ’s. We achieve this by learning the function r via monotonic neural networks. Since $\text{PIT}(y; \mathbf{x}) < \gamma \iff y \in (-\infty, \hat{F}^{-1}(\gamma|\mathbf{x}))$, the L^2 loss function used for training directly encourages conditional calibration. Moreover, our procedure is amortized, in the sense that we can train on \mathbf{x} and γ jointly, after which the function r can be evaluated for any \mathbf{x} ’s and γ . By evaluating how far $r^{\hat{F}}(\gamma; \mathbf{x})$ is from γ , one can assess at what locations in feature space \hat{F} is well-estimated. Moreover, the learnt function $\hat{r}^{\hat{F}}(\gamma; \mathbf{x})$ itself suggests *how* \hat{F} can be adjusted; that is, we are providing the practitioner with both interpretable diagnostics and a means for correcting discrepancies.

Relation to Other Work

Goodness-of-fit tests and calibration: Goodness-of-fit of PDs to observed data can be assessed by two-sample tests [Stute and Zhu, 2002, Moreira, 2003, Jitkrittum et al., 2020b]. Such tests are useful for deciding whether a PD needs to be improved, but do not provide any means to correct discrepancies. One way to recalibrate PDs to fit data on average is to instead assess how the marginal distribution of the PIT values differs from a uniform distribution [Cook et al., 2006, Freeman et al., 2017, Talts et al., 2018, D’Isanto and Polsterer, 2018] and apply corrections to bring them into agreement [Bordoloi et al., 2010]; by construction, such recalibration schemes only improve marginal calibration. In this work, we instead build on Zhao et al. [2021], which proposes a version of PIT that is determined across the entire input feature space.

Quantile regression: Quantile regression intervals converge to the oracle $C_\alpha^*(\mathbf{X}) = [F^{-1}(0.5\alpha|\mathbf{X}), F^{-1}(1 - 0.5\alpha|\mathbf{X})]$ [Koenker and Bassett Jr., 1978, Taylor and Bunn, 1999]. Even though $C_\alpha^*(\mathbf{X})$ satisfies Equation 1, the standard pinball loss can yield highly miscalibrated UQ models for finite data sets [Chung et al., 2021b, Feldman et al., 2021]. New loss functions have been proposed to address this issue [Chung et al., 2021b, Feldman et al., 2021]. Our approach also provides calibrated prediction regions but is more general — yielding full PDs, and not only prediction intervals.

Conformal inference: Conformal prediction methods have the appealing property of yielding prediction sets with finite-sample marginal validity, $\mathbb{P}(Y \in C(\mathbf{X})) \geq 1 - \alpha$, as long as

the data are exchangeable [Vovk et al., 2005, Lei et al., 2018]. However, there is no guarantee that Equation 1 is satisfied, even approximately. More recent efforts have addressed approximate conditional validity [Romano et al., 2019, Izbicki et al., 2020, Chernozhukov et al., 2021, Izbicki et al., 2022] by designing conformal scores with an approximately homogeneous distribution across \mathcal{X} . Unfortunately, it is difficult to check whether these methods provide good conditional coverage in practice. Conformal prediction bands are also not conditionally valid, even asymptotically, if the initial model is misspecified. Finally, unlike conformal inference, our method provides estimates of the full PD.

Contribution and Novelty

We present a unified framework for diagnostics and recalibration of *entire predictive distributions* $F(y|\mathbf{x})$; see, e.g., Section 5.2 for an application to a high-impact physics problem that requires good estimates of multimodal distributions. Our method directly targets conditional coverage and provides interpretable diagnostics, with well-calibrated prediction sets as a by-product of our PDs. Although estimating entire distributions nonparametrically is difficult, our methods’s performance, in terms of conditional coverage and efficiency (i.e. tight regions), is on par with state-of-the-art predictive inference algorithms for constructing prediction sets; see Section 4.1 for comparisons. Our method can handle *model mis-specifications*; see Section 4.2 for an example of diagnostics and recalibration in a setting with distributional shift. Finally, our framework can be applied to stationary time series and other settings with *dependent* high-dimensional data; see Section 5.1 for an example with probabilistic nowcasting based on sequences of images.

2 Methodology

Notation and Objectives. Suppose that $\hat{f}(y|\mathbf{x})$ is a conditional density estimate (CDE) of a continuous random variable $Y \in \mathcal{Y} \subseteq \mathbb{R}$ given a random vector $\mathbf{X} \in \mathcal{X} \subseteq \mathbb{R}^d$. Let $\mathcal{D} = \{(\mathbf{X}_1, Y_1), \dots, (\mathbf{X}_n, Y_n)\}$ denote an i.i.d. sample from $F_{\mathbf{X}, Y}$, the joint distribution of (\mathbf{X}, Y) . Our goal is to use \mathcal{D} to recalibrate our CDE, so as to achieve correct conditional coverage. We refer to \mathcal{D} as “calibration data”, which are independent from the “train data” used to construct $\hat{f}(y|\mathbf{x})$.

Local Diagnostics via PIT

Our calibration framework uses diagnostics developed by Zhao et al. [2021]¹ for assessing conditional density models. For fixed $\mathbf{x} \in \mathcal{X}$ and $y \in \mathcal{Y}$, the local probability integral transform (PIT) of y at \mathbf{x} is given by

$$\text{PIT}(y; \mathbf{x}) := \int_{-\infty}^y \hat{f}(y'|\mathbf{x}) dy' = \hat{F}(y|\mathbf{x}). \quad (2)$$

¹see supplementary materials

where \hat{F} is CDF associated with \hat{f} . The diagnostics require the estimation of the CDF of the PIT values, which we refer to as the PIT-CDF:

Definition 1 (PIT-CDF). For every $\mathbf{x} \in \mathcal{X}$ and $\gamma \in (0, 1)$, the CDF of the local PIT is given by

$$r^{\hat{f}}(\gamma; \mathbf{x}) := \mathbb{P}(\text{PIT}(Y; \mathbf{x}) \leq \gamma | \mathbf{x}). \quad (3)$$

We learn $r^{\hat{f}}(\gamma; \mathbf{x})$ using regression: in this paper, we first augment the calibration data \mathcal{D} by drawing $\gamma_{i,1}, \dots, \gamma_{i,K} \sim U(0, 1)$ for each data point ($i = 1, \dots, n$), then regress the random variable

$$W_{i,j} := \mathbb{I}(\text{PIT}(Y_i; \mathbf{X}_i) \leq \gamma_{i,j}) \quad (4)$$

on both \mathbf{X}_i and $\gamma_{i,j}$ using the augmented calibration sample $\mathcal{D}' = \{(\mathbf{X}_i, Y_i, W_{i,j})\}_{i,j}$, for $i = 1, \dots, n$ and $j = 1, \dots, K$. As $r^{\hat{f}}(\gamma; \mathbf{x})$ is a non-decreasing function of γ , we use monotonic neural networks [Wehenkel and Louppe, 2019] as our regression algorithm though any other suitable regression method may be used.

The PIT-CDF values $r^{\hat{f}}(\gamma; \mathbf{x})$ characterize the local consistency of \hat{f} , defined as follows:

Definition 2 (Local consistency). A density estimate $\hat{f}(\cdot|\mathbf{x})$ is locally consistent at a fixed \mathbf{x} if, and only if, $\hat{F}(\cdot|\mathbf{x}) = F(\cdot|\mathbf{x})$.

Indeed, for fixed x , $\hat{f}(\cdot|\mathbf{x})$ is locally consistent, if and only if, $r^{\hat{f}}(\gamma; \mathbf{x}) = \gamma$ for every $\gamma \in (0, 1)$ [Zhao et al., 2021, Corollary 1]. Hence, by plotting an estimate of $r^{\hat{f}}(\gamma; \mathbf{x})$ versus γ , referred to as Amortized Local P-P plots (ALPs), we can assess how close \hat{f} is to f across the entire feature space. We can also describe the type of deviations that might occur; see Figure 4 for some examples.

Cal-PIT

Cal-PIT uses the estimated regression function $\hat{r}^{\hat{f}}(\gamma; \mathbf{x}) := \hat{\mathbb{P}}(\text{PIT}(Y; \mathbf{x}) \leq \gamma | \mathbf{x})$ to correct the original CDE \hat{f} , so that the recalibrated CDE \tilde{f} is approximately locally consistent across the feature space. The procedure is as follows: Consider a fixed evaluation point \mathbf{x} and $\gamma \in G$, where G is a fine grid over $(0, 1)$. Let $\beta := \hat{r}^{\hat{f}}(\gamma; \mathbf{x})$. If the regression is perfectly estimated (that is, $\hat{r}^{\hat{f}} = r^{\hat{f}}$), then, as long as both F and \hat{F} are continuous and \hat{F} dominates F (see Assumptions 1 and 2 in Section 3 for details),

$$\beta := r^{\hat{f}}(\gamma; \mathbf{x}) = \mathbb{P}\left(Y \leq \hat{F}^{-1}(\gamma | \mathbf{x}) \mid \mathbf{x}\right). \quad (5)$$

That is, the probability of observing the response variable Y below a predicted γ -quantile at x is equal to β . However, local consistency at \mathbf{x} requires this probability to be equal to γ .

The above result suggests that we “adjust” the values of \hat{F} , and define a new cumulative (conditional) distribution function \tilde{F} , where

$$\tilde{F}^{-1}(\beta|\mathbf{x}) := \hat{F}^{-1}(\gamma|\mathbf{x}). \quad (6)$$

By Equations 5-6, the new CDE \tilde{f} will then satisfy the local consistency condition:

$$r^{\tilde{f}}(\gamma; \mathbf{x}) := \mathbb{P}\left(Y \leq \tilde{F}^{-1}(\gamma|\mathbf{x}) \mid \mathbf{x}\right) = \gamma.$$

Finally, for each \mathbf{x} of interest, we use splines to interpolate between γ -values on the grid G , so that $\tilde{F}^{-1}(\cdot|\mathbf{x})$ and $\tilde{F}(\cdot|\mathbf{x})$ can be evaluated for all $\beta \in (0, 1)$. The Cal-PIT prediction interval at \mathbf{x} , defined as

$$C_\alpha(\mathbf{x}) := \left[\tilde{F}^{-1}(0.5\alpha|\mathbf{x}), \tilde{F}^{-1}(1 - 0.5\alpha|\mathbf{x}) \right],$$

approximately achieves $1 - \alpha$ conditional coverage. Alternatively, one may use Highest Predictive Density (HPD) sets, defined as $C_\alpha(\mathbf{x}) = \{y : \tilde{f}(y|\mathbf{x}) \geq \tilde{t}_{\mathbf{x},\alpha}\}$, where $\tilde{t}_{\mathbf{x},\alpha}$ is such that $\int_{y \in C_\alpha(\mathbf{x})} \tilde{f}(y|\mathbf{x}) dy = 1 - \alpha$ and \tilde{f} is the density associated to \tilde{F} . HPD regions can produce more informative and considerably smaller prediction sets than intervals for multimodal and skewed densities. See Appendix A for additional details.

Algorithm 1 (in Appendix B) details the Cal-PIT procedure for constructing either prediction intervals or recalibrated CDEs from F^{-1} .

Remark 1. *If the initial model is good, then r is easy to estimate; for instance, $\hat{f} = f$ implies a constant function $r^{\hat{f}}(\gamma; \mathbf{x}) = \gamma$. However, \hat{f} needs to cover the whole space. Depending on the application, an estimate of the marginal distribution $f(y)$, or an initial fit with an MDN and a wide Gaussian (see Examples 5.1), could both be viable options.*

3 Theoretical Properties

Next, we provide convergence rates for the recalibrated CDF estimator \tilde{F} , and show that Cal-PIT intervals achieve asymptotic conditional validity even if the initial CDE \hat{f} is not consistent. The following results are conditional on \hat{f} ; all uncertainty refers to the calibration sample. We assume that the true distribution of $Y|\mathbf{x}$ and its initial estimate are continuous, and that \hat{F} places its mass on a region that is at least as large as that of F :

Assumption 1 (Continuity of the cumulative distribution functions). *For every $\mathbf{x} \in \mathcal{X}$, $\hat{F}(\cdot|\mathbf{x})$ and $F(\cdot|\mathbf{x})$ are strictly continuous functions.*

Assumption 2 (\hat{F} dominates F). *For every $\mathbf{x} \in \mathcal{X}$, $\hat{F}(\cdot|\mathbf{x})$ dominates $F(\cdot|\mathbf{x})$.*

To provide convergence rates for the recalibrated CDF, we assume that $F(\cdot|\mathbf{x})$ cannot place too much mass in regions where the initial estimate $\hat{F}(\cdot|\mathbf{x})$ places little mass:

Assumption 3 (Bounded density). *There exists $K > 0$ such that, for every $\mathbf{x} \in \mathcal{X}$, the Radon-Nikodym derivative of $F(\cdot|\mathbf{x})$ with respect to $\hat{F}(\cdot|\mathbf{x})$ is bounded above by K .*

Finally, we assume that the regression method converges at a rate $O(n^{-\kappa})$:

Assumption 4 (Convergence rate of the regression method). *The regression method used to estimate $r^{\hat{f}}$ is such that its convergence rate is given by*

$$\mathbb{E} \left[\int \int \left(\hat{r}^{\hat{f}}(\gamma; \mathbf{x}) - r^{\hat{f}}(\gamma; \mathbf{x}) \right)^2 d\gamma dP(\mathbf{x}) \right] = O\left(\frac{1}{n^\kappa}\right)$$

for some $\kappa > 0$.

Many methods satisfy Assumption 4 for some value κ , which is typically related to the dimension of \mathcal{X} and the smoothness of the true regression r (see for instance Györfi et al. 2002).

Under these assumptions, we can derive the rate of convergence for \tilde{F} :

Theorem 1. *Under Assumptions 1, 2, 3 and 4,*

$$\mathbb{E} \left[\int \int \left(\tilde{F}(y|\mathbf{x}) - F(y|\mathbf{x}) \right)^2 dP(y, \mathbf{x}) \right] = O\left(\frac{1}{n^\kappa}\right).$$

Next, we show that with an uniformly consistent regression estimator $\hat{r}^{\hat{f}}(\gamma; \mathbf{x})$ (see Bierens 1983, Hardle et al. 1984, Liero 1989, Girard et al. 2014 for some examples), Cal-PIT intervals achieve asymptotic conditional validity, even if the initial CDE $\hat{f}(y|\mathbf{x})$ is not consistent.

Assumption 5 (Uniform consistency of the regression estimator). *The regression estimator is such that*

$$\sup_{\mathbf{x} \in \mathcal{X}, \gamma \in [0,1]} |\hat{r}^{\hat{f}}(\gamma; \mathbf{x}) - r^{\hat{f}}(\gamma; \mathbf{x})| \xrightarrow[n \rightarrow \infty]{a.s.} 0,$$

where the convergence is with respect to the calibration set \mathcal{D} only; \hat{f} is fixed.

Theorem 2 (Consistency and conditional coverage of Cal-PIT intervals). *Let $C_\alpha^*(\mathbf{x}) = [F^{-1}(0.5\alpha|\mathbf{x}); F^{-1}(1 - 0.5\alpha|\mathbf{x})]$ be the oracle prediction band, and let $C_\alpha^n(\mathbf{x})$ denote the Cal-PIT interval. Under Assumptions 1, 2 and 5,*

$$\lambda(C_\alpha^n(\mathbf{X}) \Delta C_\alpha^*(\mathbf{X})) \xrightarrow[n \rightarrow \infty]{a.s.} 0,$$

where λ is the Lebesgue measure in \mathbb{R} and Δ is the symmetric difference between two sets. It follows that $C_\alpha^n(\mathbf{X})$ has asymptotic conditional coverage of $1 - \alpha$ [Lei et al., 2018].

See Appendix C.1 for theoretical results for cal-PIT(HPD).

4 Toy Examples

Our primary goal is to calibrate entire PDs, but because of the rich literature on constructing calibrated prediction sets,

we here benchmark `cal-PIT` prediction sets against results from state-of-the-art quantile regression and conformal inference methods, in addition to comparing our results to oracle bands from Monte Carlo (MC) simulations from the true data-generating process (DGP).

We study two toy examples with and without model misspecifications (due to distributional shift).

4.1 Example 1: IID Data. No Model Misspecification.

Our first example is a low-dimensional toy version of the galaxy photometric redshift (photo- z) application in Section 5.2, for which we expect the PDs to be multimodal in some parts of the feature space, as multiple widely different distances (redshifts) can be consistent with the observed features (colors) of a galaxy. Motivated by the photo- z application, we modify the two-group example of Feldman et al. [2021] to have a bimodal structure. Appendix D details the DGP. In our example, the target variable Y depends on three variables (X_0, X_1, X_2), with one of the variables (X_0) indicating group membership.

However, the practitioner only has access to the predictors X_1 and X_2 , resulting in the CDE being bimodal in the regime $X_1 > 0$ with one branch for each class (see “Majority” versus “Minority” in Figure 1).

For benchmarking purposes, we compute 90% prediction sets for Y with `Cal-PIT (INT)` and `Cal-PIT (HPD)`, and then compare the results to prediction sets from five state-of-the-art methods, namely: (i) quantile regression (QR; Koenker and Bassett Jr. 1978) with a pinball loss; (ii) conformalized quantile regression (CQR; Romano et al. 2019); (iii) orthogonal quantile regression (OQR; Feldman et al. 2021) which introduces a penalty on the pinball loss to improve conditional coverage; (iv) `Reg-split` [Lei et al., 2018]; and (v) distributional conformal prediction (DCP; Chernozhukov et al. 2021). Methods (i)-(iv) are all trained with XGBoost [Chen and Guestrin, 2016]. Our `Cal-PIT` methods use an initial CDE trained using FlexCode with an XGBoost regressor [Izbicki and Lee, 2017, Dalmaso et al., 2020] and a monotonic neural network [Wehenkel and Louppe, 2019] for learning $\hat{r}^f(\gamma; \mathbf{x})$. Finally, DCP computes a conformal score based on PIT values derived from the same initial CDE as `Cal-PIT`.

We split data of total size n equally into train and calibration sets (except for QR and OQR which use all data for training). As we know the true DGP for the synthetic data, we can use MC simulations to compute the true conditional coverage at a fixed set of 1000 uniformly sampled test points in \mathbf{X} . Similarly, we can compute “oracle” prediction sets.

Figure 2 compares the conditional coverage of each method. Test points with coverage within two standard deviations (SD) of $1 - \alpha = 0.9$ based on 100 random realizations are labeled as having “correct” coverage. All methods improve

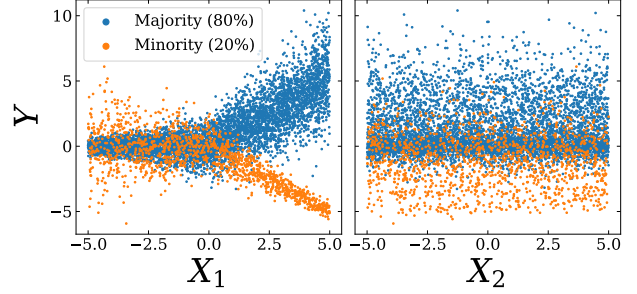


Figure 1: Visualization of one random instance of the data used for Example 1. There are two covariates (X_1, X_2), and a target variable Y . The analytic form of the true data distribution is defined in Appendix D. The data set consists of two groups with different spreads. Y splits into two branches for $X_1 > 0$; that is, the true CDE is bimodal in this region.

in terms of conditional coverage with increasing sample size, but only `Cal-PIT` consistently attains the nominal 90% coverage across the feature space for $n \geq 2000$.

Figure 3 shows the calibrated CDEs from `Cal-PIT`. These estimates reveal that the true conditional density is bimodal for $X_1 > 0$; thus, the most efficient prediction sets in this feature subspace would not be single intervals, but rather pairs of intervals. Indeed, Fig. 8 shows that `Cal-PIT (HPD)` yields smaller prediction sets than `Cal-PIT (INT)`. Because HPD sets can capture the bimodality in the data while intervals cannot, this is a case where `Cal-PIT (HPD)` has better efficiency. This qualitative insight is only possible because `Cal-PIT` estimates the entire PDs.

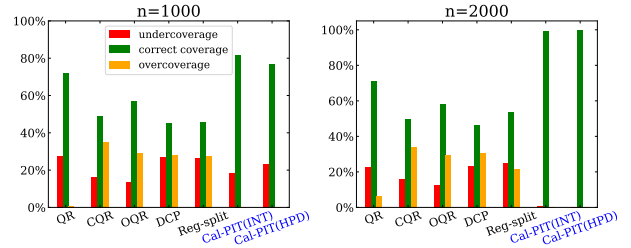


Figure 2: The proportion of test points with correct conditional coverage for different methods. Data of total size n are split equally into train and calibration sets (except for QR which uses all data for training). While conformal methods improve upon QR, `Cal-PIT` leads to better conditional coverage, even for smaller sample sizes.

4.2 Example 2: Mis-specified Models

The next example demonstrates that our method can effectively diagnose and correct model mis-specifications, yielding prediction sets that still achieve conditional coverage. We explore a problem with a single predictor X in two different settings: One in which the true target distribution f is skewed and a second for which f is kurtotic. In both

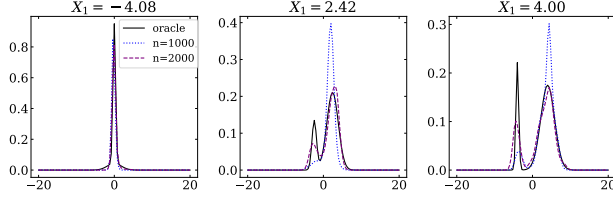


Figure 3: Conditional PDFs for sample points at different locations of X_1 . The true “oracle” PDF is bimodal for $X_1 > 0$; thus, the most efficient prediction sets in this feature subspace are not single intervals, but pairs of intervals. Cal-PIT estimates entire PDs, which converge to oracle PDs as the sample size increases.

cases, the initial estimate of the distribution, \hat{f} (used for the inputs to Cal-PIT) is a Gaussian centered on the true conditional mean with a standard deviation of 2 units. We split the data evenly between training and calibration sets with each having 10,000 data points. Using a monotonic neural network regression function for local PIT coverage trained on the calibration set, $\hat{r}^f(\gamma; \mathbf{x})$, we construct “amortized local P-P plots” (ALPs) to show *how* the estimated conditional density $\hat{f}(y|x)$ deviates from the true density in each setting (center panel of Fig. 4). We then use Cal-PIT to recalibrate the initial predictions.

We draw samples from the true DGPs (see Appendix D for details) to assess the conditional coverage for various values of X on an independent test set as shown in the right panel of Fig. 4. The PDs achieve nominal conditional coverage after recalibration using Cal-PIT whereas reg-split, CQR and DCP fail to achieve conditional coverage, even though they are calibrated using data from the true data-generating process. Our method is the only one that pinpoints the nature of the discrepancy from the estimated distribution and then directly corrects for deviations in conditional coverage.

5 Applications

5.1 Probabilistic Nowcasting for Dependent High-Dimensional Data

Next we illustrate Cal-PIT calibration of entire PDs of $Y_t | \mathbf{S}_{<t}$ for high-dimensional sequence data $\{(\mathbf{S}_{<t}, Y_t)\}$, which are based on satellite images of tropical cyclones (TCs). The target variable Y_t represents TC intensity at time t , and the predictor $\mathbf{S}_{<t}$ is an entire 24-hour sequence of one-dimensional functions summarizing the spatio-temporal evolution of TC convective structure leading up to time t . The sequence data are strongly correlated as the image sequences from time t to $t+1$ are only shifted by 30 minutes.

For this example, we simulate from a model fit to observed data so that we can compute exact conditional coverage; the details are in Appendix G. The original data capture TC convective structure, as observed every 30 minutes by Geostationary Operational Environmental Satellite (GOES)

infrared imagery [Janowiak et al., 2020] of storms from the North Atlantic and Eastern North Pacific basins between 2000-2020; in addition, we have TC intensities from NHC’s HURDAT2 best track database (6-hour synoptic times are interpolated for a 30-minute resolution before fitting a vector-autoregressive model; we then simulate a series of scalar TC intensities Y_t via a time series regression of Y_t on its own most recent values and on $\mathbf{S}_{<t}$).

Figure 5 shows an example of data from a simulated storm. On the left, we have a so-called Hovmöller diagram of the evolution of TC convective structure $\{(\mathbf{X}_t)\}_{t \geq 0}$, with each row representing the radial profile $\mathbf{X}_t \in \mathbb{R}^{120}$ of cloud-top temperatures as a function of radial distance from the TC center; time evolution is top-down in hours.

On the right, we have $\{Y_t\}_{t \geq 0}$, the simulated TC “intensities” at corresponding times t . Let a sequence $\mathbf{S}_{<t} := (\mathbf{X}_{t-48}, \mathbf{X}_{t-47}, \dots, \mathbf{X}_t)$ include the 24-hour history of convective structure (49 radial profiles). We simulate 800 “storms” from a fitted TC length distribution. Sequence data $\{(\mathbf{S}_{<t}, Y_t)\}$ from the same storm are shifted by 30 minutes; hence, they are *strongly correlated*. Sequence data from different storms, on the other hand, are independent.

Our goal is to construct prediction sets for $Y_t | \mathbf{S}_{<t}$, and illustrate how Cal-PIT improves upon an initial MDN fit. Train, calibration, and testing were performed on *different* simulated “storms”. First, we fit an initial CDE (ConvMDN; D’Isanto and Polsterer 2018), which estimates $f(y|s)$ as a unimodal Gaussian, using a train set with 8000 points, $\{(\mathbf{S}_{<t}, Y_t)\}$ (see Appendix G for details). Next, we apply Cal-PIT to learn $\hat{r}^f(\gamma; \mathbf{s})$ using 8000 calibration points. Note however that the data within the same storm are *highly* dependent; hence, the effective train or calibration sample sizes are much smaller than the nominal value. Finally, we evaluate the conditional coverage of the initial CDE and Cal-PIT on 4000 test points; see Fig. 6. Cal-PIT recalibration improves upon the initial ConvMDN fit: Fig. 6 (left) shows prediction sets for $Y_t | \mathbf{S}_{<t}$ for a sample simulated TC, before and after calibration. The calibrated prediction sets track the behavior of the observed trajectory more closely, as shown in Appendix G. Moreover, the right panel shows Cal-PIT achieves better conditional coverage, even though the effective sample size is small because of dependencies between intensities in the same storm.

5.2 Calibrating CDEs of Galaxy Distance

Next we apply our method for photo- z estimation. Redshift (z) is a measure of distance to a galaxy and is crucial for astrophysics and cosmology. However, obtaining direct redshift measurements of a large number of objects is prohibitively resource-intensive. Therefore, redshift estimates often must be derived from easier-to-obtain imaging data, resulting in measurements called photometric redshifts or photo- z ’s. We have chosen this application because of

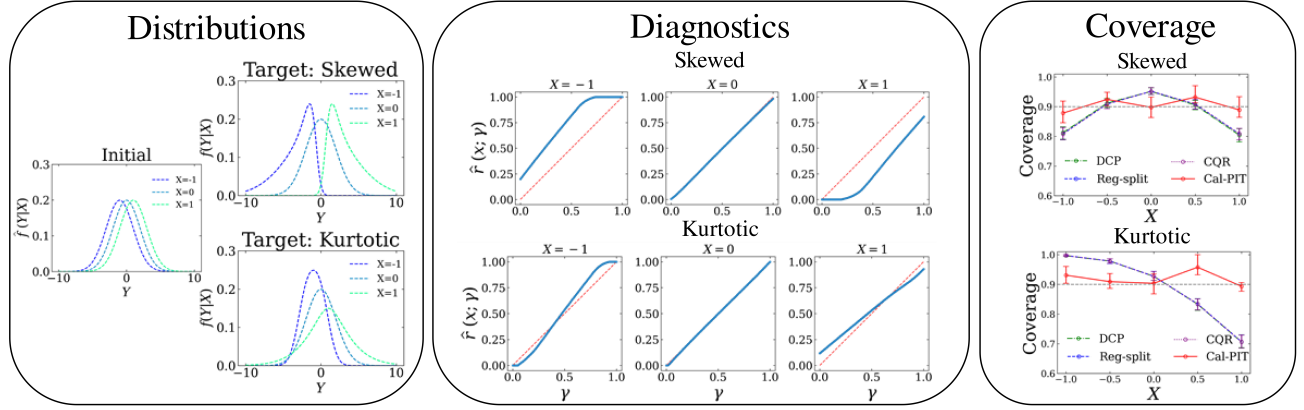


Figure 4: *Left*: Initial and target distributions for Example 4.2. The initial fit is Gaussian, but the target distributions are skewed and kurtotic, so the model is mis-specified. Conditional densities for each distribution are shown at slices of X . *Center*: Diagnostic local P-P plots. Cal-PIT identifies that, relative to the training density, the skewed observed data are biased at $X = -1/X = 1$ but well estimated at $X = 0$, and that the observed data for the kurtotic target are well estimated at $X = 0$ but under- or over-dispersed at $X = -1/X = 1$. These insights allow Cal-PIT to correct the initial model. *Right*: Conditional coverage obtained via different calibration methods on target data; nominal coverage level $1 - \alpha = 0.9$. Cal-PIT is the only method to achieve conditional validity for all inputs X .

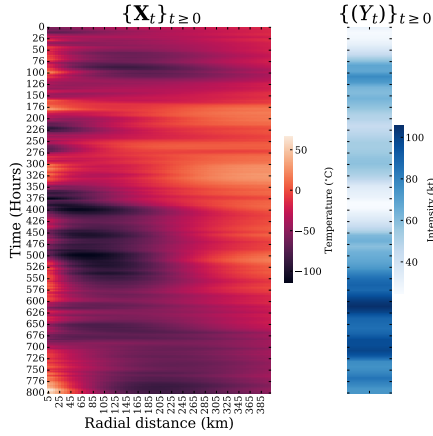


Figure 5: Simulated radial profiles and intensities for an example TC. *Left*: Hovmöller diagram of the evolution of TC convective structure $\{X_t\}_{t \geq 0}$; each row represents the radial profile X_t of cloud-top temperatures as a function of radial distance from the TC center at time t . Our predictors are 48-hour overlapping sequences $\{S_t\}_{t \geq 0}$ with data from the same “storm” being highly dependent. *Right*: The target response, here shown as a time series $\{(Y_t)\}_{t \geq 0}$ of simulated TC intensities.

its high impact in science, and because the photo- z data challenge (DC1) of Schmidt et al. [2020] is providing clear benchmarks against state-of-the-art CDE methods.

Multimodality or degenerate solutions occur because images contain limited information about redshifts. Consequently, galaxies at very different redshifts can have similar image properties. CDEs are commonly used to represent photo- z estimates and associated uncertainties; the PDs are often multi-modal (because of degeneracies), and do not conform to any of the standard models [Benítez, 2000, Mandelbaum

et al., 2008, Malz and Hogg, 2022]. Machine learning-based methods are widely used to predict photo- z -distributions when adequate training data are available (e.g., [Beck et al., 2016, Zhou et al., 2021, Dalmasso et al., 2020, Almosallam et al., 2016, Dey et al., 2021]), though they do not guarantee accurate conditional coverage.

Here we use the simulated data from Schmidt et al. [2020], which has been used to benchmark photo- z CDE prediction methods in the past. The features used to train the models are called apparent magnitudes and colors which are various measures of total light in an image. We use the “training set” from Schmidt et al. [2020] with about 44,000 instances as our calibration set; then split the remaining data into two sets: a validation set (twice as large as the calibration set) and a larger test set comprised of roughly 250,000 instances. We start with the marginal distribution of redshifts as our initial CDE estimate. Schmidt et al. [2020] demonstrated that such a CDE estimate can perform well on many commonly used metrics that check for marginal coverage, although it does not provide information about individual instances.

We learn the local distribution of PIT values by training $r\hat{f}$ on the calibration set and use it to recalibrate the CDEs in our validation and test sets using the methods described in Section 2. To assess the quality of our recalibrated CDEs, we train another regression model using the validation set and its recalibrated CDEs. We also use the CDE loss [Izbicki and Lee, 2017] as another independent metric of conditional coverage. We infer the local CDF of PIT for every instance in the test set before and after recalibration using the two trained models. Fig. 7 (top) shows the diagnostic local P-P plot for three galaxies in the test set. The local CDF of PIT for these instances follows the identity line closely (i.e., the CDF of a uniform distribution), indicating good conditional coverage. Fig. 7 (bottom) also shows that multimodal CDEs

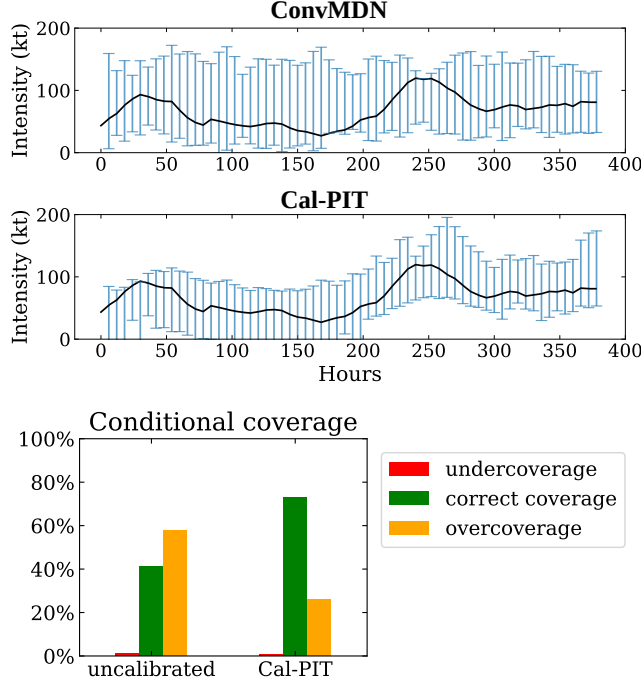


Figure 6: *Top*: Simulated TC example with dependent high-dimensional sequence data. Prediction sets for TC intensities, before and after calibration (blue bars), together with the actual trajectory of intensities $\{Y_t\}_t$ (solid black lines). Cal-PIT tracks the behavior of the trajectories more closely. *Bottom*: Conditional coverage of both methods across sequences s . The initial ConvMDN fit with a single Gaussian component over-covers in certain regions of the feature space due to the true PD being skewed toward larger intensities (Appendix G); Cal-PIT partly corrects for the over-coverage and returns more precise prediction sets.

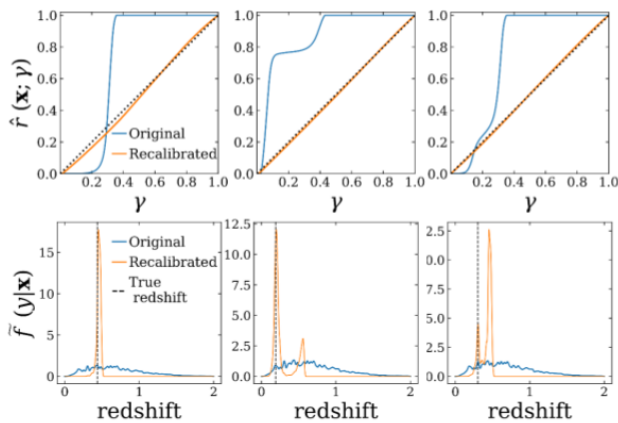


Figure 7: *Top*: Diagnostic local P-P plot for three galaxies before and after Cal-PIT is applied. *Bottom*: CDEs for the corresponding galaxies before and after calibration along with their true redshifts. Recalibration using Cal-PIT can recover multimodalities while ensuring good conditional coverage.

Table 1: Comparison with methods benchmarked in the LSST-DESC Photo-z Data Challenge [Schmidt et al., 2020]. In terms of CDE loss, Cal-PIT performs better than all the other methods compared including one approach which was specifically optimized for minimum CDE loss (FlexZBoost).

Photo-z Algorithm	CDE Loss
ANNz2 [Sadeh et al., 2016]	-6.88
BPZ [Benítez, 2000]	-7.82
Delight [Leistedt and Hogg, 2017]	-8.33
EAZY [Brammer et al., 2008]	-7.07
FlexZBoost [Izbicki and Lee, 2017]	-10.60
GPz [Almosallam et al., 2016]	-9.93
LePhare [Arnouts et al., 1999]	-1.66
METAPhoR [Cavuoti et al., 2017]	-6.28
CMNN [Graham et al., 2018]	-10.43
SkyNet [Graff et al., 2014]	-7.89
TPZ [Carrasco Kind and Brunner, 2013]	-9.55
trainZ [Schmidt et al., 2020]	-0.83
Cal-PIT	-10.71

even when the input CDE before calibration is unimodal. We also see a large improvement in the value of the CDE Loss, with a decrease from -0.84 to -10.71 after recalibration. Table 1 shows that Cal-PIT yields lower CDE loss than any of the cutting-edge methods benchmarked by [Schmidt et al., 2020] as part of the LSST-DESC data challenge. The Cramér-von Mises statistic between the local PIT CDF and the uniform distribution is another measure of the quality of conditional coverage [Schmidt et al., 2020], and decreases significantly on the entire test set when comparing both fits, with a mean decrease of $\sim 4.5\times$ (App. E).

6 Discussion

Whereas there are few reliable estimators for conditional densities or quantile regression, there is a large literature devoted to estimating regression functions. Our approach draws upon the success of such literature to create corrections for PDs with a minimum of assumptions.

Cal-PIT can assess whether a PD estimate $\hat{F}(\cdot|x)$ is well-calibrated for all inputs x , as well as correct for discrepancies. In order for Cal-PIT corrections to give good results, the initial estimate $\hat{F}(\cdot|x)$ needs to place its mass on a region which is at least as large as $F(\cdot|x)$,² but the initial fit can be poor otherwise. Good results also require calibration data to learn the regression function (Eq. 3); empirically, we see that data sizes are still reasonable if using the right NN architecture and training correctly. Cal-PIT does not require exchangeable data, only stationary processes; hence it can be applied to (stationary) probabilistic time series forecasting. Individually calibrated PDs automatically

²if this is not the case, a practical way of mitigating the problem is by artificially widening \hat{F} by convolving with a Gaussian kernel

can be recovered (as are typical for photo- z 's, cf. App. E),

return conditionally calibrated prediction sets. However, Cal-PIT works under the assumption that Y is continuous and does not apply to classification tasks (unlike calibration schemes in, e.g., Kull et al. 2019, Wald and Globerson 2017).

Finally, Cal-PIT can potentially be extended to multivariate output vectors \mathbf{Y} by the decomposition $f(\mathbf{y}|\mathbf{x}) = \prod_i f(y_i|\mathbf{x}, \mathbf{y}_{<i})$; thus performing Cal-PIT corrections on auto-regressive components of the conditional distribution. This is a particularly promising direction for Deep Pixel-CNN and Pixel-RNN models [Van den Oord et al., 2016, van den Oord and Kalchbrenner, 2016] (work in progress).

Acknowledgments

The authors would like to thank Trey McNeely for helpful discussions and for preparing the tropical cyclone data that were used to fit the Example 3 model. This work is supported in part by NSF DMS-2053804, NSF PHY-2020295, and the C3.ai Digital Transformation Institute. BD, BHA and JAN acknowledge the support of the National Science Foundation under Grant No. AST-2009251. Any opinions, findings, and conclusions or recommendations expressed in this material are those of the author(s) and do not necessarily reflect the views of the National Science Foundation. RI is grateful for the financial support of CNPq (309607/2020-5 and 422705/2021-7) and FAPESP (2019/11321-9). This research used resources of the National Energy Research Scientific Computing Center (NERSC), a U.S. Department of Energy Office of Science User Facility located at Lawrence Berkeley National Laboratory, operated under Contract No. DE-AC02-05CH11231.

References

- Moloud Abdar, Farhad Pourpanah, Sadiq Hussain, Dana Rezazadegan, Li Liu, Mohammad Ghavamzadeh, Paul Fieguth, Xiaochun Cao, Abbas Khosravi, U. Rajendra Acharya, Vladimir Makarenkov, and Saeid Nahavandi. A review of uncertainty quantification in deep learning: Techniques, applications and challenges. *Inf. Fusion*, 76 (C):243–297, dec 2021. ISSN 1566-2535. doi: 10.1016/j.inffus.2021.05.008. URL <https://doi.org/10.1016/j.inffus.2021.05.008>.
- Leontine Alkema, Adrian E Raftery, and Samuel J Clark. Probabilistic projections of hiv prevalence using bayesian melding. *The annals of applied statistics*, 1(1):229–248, 2007.
- Ibrahim A. Almosallam, Matt J. Jarvis, and Stephen J. Roberts. GPZ: non-stationary sparse Gaussian processes for heteroscedastic uncertainty estimation in photometric redshifts. *MNRAS*, 462(1):726–739, October 2016. doi: 10.1093/mnras/stw1618.
- Luca Ambrogioni, Umut Güçlü, Marcel A. J. van Gerven, and Eric Maris. The Kernel Mixture Network: A Non-parametric Method for Conditional Density Estimation of Continuous Random Variables. *arXiv e-prints*, art. arXiv:1705.07111, May 2017.
- Ilaria Lucrezia Amerise. Quantile regression estimation using non-crossing constraints. *Journal of Mathematics and Statistics*, 14(1):107–118, May. 2018. doi: 10.3844/jmssp.2018.107.118. URL <https://thescipub.com/abstract/jmssp.2018.107.118>.
- S. Arnouts, S. Cristiani, L. Moscardini, S. Matarrese, F. Lucchin, A. Fontana, and E. Giallongo. Measuring and modelling the redshift evolution of clustering: the Hubble Deep Field North. *MNRAS*, 310(2):540–556, December 1999. doi: 10.1046/j.1365-8711.1999.02978.x.
- Elizabeth A Barnes, Randal J Barnes, and Nicolas Gordillo. Adding uncertainty to neural network regression tasks in the geosciences. *arXiv preprint arXiv:2109.07250*, 2021.
- Róbert Beck, László Dobos, Tamás Budavári, Alexander S. Szalay, and István Csabai. Photometric redshifts for the SDSS Data Release 12. *MNRAS*, 460(2):1371–1381, August 2016. doi: 10.1093/mnras/stw1009.
- Narciso Benítez. Bayesian Photometric Redshift Estimation. *ApJ*, 536(2):571–583, June 2000. doi: 10.1086/308947.
- James O. Berger and Leonard A. Smith. On the statistical formalism of uncertainty quantification. *Annual Review of Statistics and Its Application*, 6(1):433–460, 2019. doi: 10.1146/annurev-statistics-030718-105232. URL <https://doi.org/10.1146/annurev-statistics-030718-105232>.
- Herman J Bierens. Uniform consistency of kernel estimators of a regression function under generalized conditions. *Journal of the American Statistical Association*, 78(383): 699–707, 1983.
- Christopher M. Bishop. Mixture density networks. 1994. URL <https://publications.aston.ac.uk/id/eprint/373/>.
- R. Bordoloi, S. J. Lilly, and A. Amara. Photo-z performance for precision cosmology. *Monthly Notices of the Royal Astronomical Society*, 406(2):881–895, 08 2010. URL <https://doi.org/10.1111/j.1365-2966.2010.16765.x>.
- Gabriel B. Brammer, Pieter G. van Dokkum, and Paolo Coppi. EAZY: A Fast, Public Photometric Redshift Code. *ApJ*, 686(2):1503–1513, October 2008. doi: 10.1086/591786.
- Matias Carrasco Kind and Robert J. Brunner. TPZ: photometric redshift PDFs and ancillary information by using prediction trees and random forests. *MNRAS*, 432(2): 1483–1501, June 2013. doi: 10.1093/mnras/stt574.
- S. Cavuoti, V. Amaro, M. Brescia, C. Vellucci, C. Tortora, and G. Longo. METAPHOR: a machine-learning-based

- method for the probability density estimation of photometric redshifts. *MNRAS*, 465(2):1959–1973, February 2017. doi: 10.1093/mnras/stw2930.
- Thomas Y. Chen, Biprateep Dey, Aishik Ghosh, Michael Kagan, Brian Nord, and Nesar Ramachandra. Interpretable Uncertainty Quantification in AI for HEP. *Proceedings of the US Community Study on the Future of Particle Physics (Snowmass 2021)*, art. arXiv:2208.03284, August 2022.
- Tianqi Chen and Carlos Guestrin. XGBoost: A scalable tree boosting system. In *Proceedings of the 22nd ACM SIGKDD International Conference on Knowledge Discovery and Data Mining, KDD '16*, pages 785–794, New York, NY, USA, 2016. ACM. ISBN 978-1-4503-4232-2. doi: 10.1145/2939672.2939785. URL <http://doi.acm.org/10.1145/2939672.2939785>.
- Victor Chernozhukov, Kaspar Wüthrich, and Yinchu Zhu. Distributional conformal prediction. *Proceedings of the National Academy of Sciences*, 118(48), 2021.
- Youngseog Chung, Willie Neiswanger, Ian Char, and Jeff Schneider. Beyond pinball loss: Quantile methods for calibrated uncertainty quantification. In Marc Aurelio Ranzato, Alina Beygelzimer, Yann N. Dauphin, Percy Liang, and Jennifer Wortman Vaughan, editors, *Advances in Neural Information Processing Systems 34: Annual Conference on Neural Information Processing Systems 2021, NeurIPS 2021, December 6-14, 2021, virtual*, pages 10971–10984, 2021a. URL <https://proceedings.neurips.cc/paper/2021/hash/5b168fdb5ee5ea262cc2d4c0b457697-Abstract.html>.
- Youngseog Chung, Willie Neiswanger, Ian Char, and Jeff Schneider. Beyond pinball loss: Quantile methods for calibrated uncertainty quantification. In *Advances in Neural Information Processing Systems*, volume 35. Curran Associates, Inc., 2021b.
- Samantha R. Cook, Andrew Gelman, and Donald B. Rubin. Validation of software for bayesian models using posterior quantiles. *Journal of Computational and Graphical Statistics*, 15(3):675–692, 2006.
- N. Dalmaso, T. Pospisil, A. B. Lee, R. Izbicki, P. E. Freeman, and A. I. Malz. Conditional density estimation tools in python and R with applications to photometric redshifts and likelihood-free cosmological inference. *Astronomy and Computing*, 30:100362, January 2020. doi: 10.1016/j.ascom.2019.100362.
- N. Dalmaso, T. Pospisil, A.B. Lee, R. Izbicki, P.E. Freeman, and A.I. Malz. Conditional density estimation tools in python and r with applications to photometric redshifts and likelihood-free cosmological inference. *Astronomy and Computing*, 30:100362, Jan 2020. ISSN 2213-1337. doi: 10.1016/j.ascom.2019.100362. URL <http://dx.doi.org/10.1016/j.ascom.2019.100362>.
- Biprateep Dey, Brett H. Andrews, Jeffrey A. Newman, Yao-Yuan Mao, Markus Michael Rau, and Rongpu Zhou. Photometric Redshifts from SDSS Images with an Interpretable Deep Capsule Network. *arXiv e-prints*, art. arXiv:2112.03939, December 2021.
- Vincent Dutordoir, Hugh Salimbeni, James Hensman, and Marc Peter Deisenroth. Gaussian process conditional density estimation. In Samy Bengio, Hanna M. Wallach, Hugo Larochelle, Kristen Grauman, Nicolò Cesa-Bianchi, and Roman Garnett, editors, *Advances in Neural Information Processing Systems 31: Annual Conference on Neural Information Processing Systems 2018, NeurIPS 2018, December 3-8, 2018, Montréal, Canada*, pages 2391–2401, 2018. URL <https://proceedings.neurips.cc/paper/2018/hash/6a61d423d02a1c56250dc23ae7ff12f3-Abstract.html>.
- Antonio D’Isanto and Kai Lars Polsterer. Photometric redshift estimation via deep learning. generalized and pre-classification-less, image based, fully probabilistic redshifts. *Astronomy & Astrophysics*, 609:A111, 2018.
- CL Farmer. Uncertainty quantification and optimal decisions. *Proceedings of the Royal Society A: Mathematical, Physical and Engineering Sciences*, 473(2200):20170115, 2017.
- Matteo Fasiolo, Simon N. Wood, Margaux Zaffran, Raphaël Nedellec, and Yannig Goude. Fast calibrated additive quantile regression. *Journal of the American Statistical Association*, 116(535):1402–1412, 2021. doi: 10.1080/01621459.2020.1725521. URL <https://doi.org/10.1080/01621459.2020.1725521>.
- Shai Feldman, Stephen Bates, and Yaniv Romano. Improving Conditional Coverage via Orthogonal Quantile Regression. *arXiv*, pages 1–20, 2021.
- Peter Freeman, Rafael Izbicki, and Ann B. Lee. A unified framework for constructing, tuning and assessing photometric redshift density estimates in a selection bias setting. *Monthly Notices of the Royal Astronomical Society*, 468(4):4556–4565, 2017. doi: 10.1093/mnras/stx764.
- Kunihiko Fukushima and Sei Miyake. Neocognitron: A new algorithm for pattern recognition tolerant of deformations and shifts in position. *Pattern Recognition*, 15(6):455–469, 1982. ISSN 0031-3203. doi: [https://doi.org/10.1016/0031-3203\(82\)90024-3](https://doi.org/10.1016/0031-3203(82)90024-3). URL <https://www.sciencedirect.com/science/article/pii/0031320382900243>.
- F. F. Gan and K. J. Koehler. Goodness-of-fit tests based on p-p probability plots. *Technometrics*, 32(3):289–303, 1990. doi: 10.1080/00401706.1990.10484682. URL <https://doi.org/10.1080/00401706.1990.10484682>.
- Stéphane Girard, Armelle Guillou, and Gilles Stupfler. Uniform strong consistency of a frontier estimator using ker-

- nel regression on high order moments. *ESAIM: Probability and Statistics*, 18:642–666, 2014.
- Xavier Glorot, Antoine Bordes, and Yoshua Bengio. Deep sparse rectifier neural networks. In Geoffrey Gordon, David Dunson, and Miroslav Dudík, editors, *Proceedings of the Fourteenth International Conference on Artificial Intelligence and Statistics*, volume 15 of *Proceedings of Machine Learning Research*, pages 315–323, Fort Lauderdale, FL, USA, 11–13 Apr 2011. JMLR Workshop and Conference Proceedings. URL <http://proceedings.mlr.press/v15/glorot11a.html>.
- Tilmann Gneiting. Probabilistic forecasting. *Journal of the Royal Statistical Society. Series A (Statistics in Society)*, pages 319–321, 2008.
- Tilmann Gneiting and Matthias Katzfuss. Probabilistic forecasting. *Annual Review of Statistics and Its Application*, 1(1):125–151, 2014. doi: 10.1146/annurev-statistics-062713-085831. URL <https://doi.org/10.1146/annurev-statistics-062713-085831>.
- Ethan Goan and Clinton Fookes. Bayesian neural networks: An introduction and survey. *CoRR*, abs/2006.12024, 2020. URL <https://arxiv.org/abs/2006.12024>.
- Simone Göttlich and Stephan Knapp. Uncertainty quantification with risk measures in production planning. *Journal of Mathematics in Industry*, 10(1):1–21, 2020.
- Philip Graff, Farhan Feroz, Michael P. Hobson, and Anthony Lasenby. SKYNET: an efficient and robust neural network training tool for machine learning in astronomy. *MNRAS*, 441(2):1741–1759, June 2014. doi: 10.1093/mnras/stu642.
- Melissa L. Graham, Andrew J. Connolly, Željko Ivezić, Samuel J. Schmidt, R. Lynne Jones, Mario Jurić, Scott F. Daniel, and Peter Yoachim. Photometric Redshifts with the LSST: Evaluating Survey Observing Strategies. *AJ*, 155(1):1, January 2018. doi: 10.3847/1538-3881/aa99d4.
- Chuan Guo, Geoff Pleiss, Yu Sun, and Kilian Q. Weinberger. On calibration of modern neural networks. In Doina Precup and Yee Whye Teh, editors, *Proceedings of the 34th International Conference on Machine Learning*, volume 70 of *Proceedings of Machine Learning Research*, pages 1321–1330. PMLR, 06–11 Aug 2017. URL <https://proceedings.mlr.press/v70/guo17a.html>.
- László Györfi, Michael Kohler, Adam Krzyzak, Harro Walk, et al. *A distribution-free theory of nonparametric regression*, volume 1. Springer, 2002.
- W Hardle, Stephan Luckhaus, et al. Uniform consistency of a class of regression function estimators. *The Annals of Statistics*, 12(2):612–623, 1984.
- Ernest Hovmöller. The trough-and-ridge diagram. *Tellus*, 1(2):62–66, 1949.
- Rafael Izbicki and Ann B Lee. Nonparametric conditional density estimation in a high-dimensional regression setting. *Journal of Computational and Graphical Statistics*, 25(4):1297–1316, 2016.
- Rafael Izbicki and Ann B Lee. Converting high-dimensional regression to high-dimensional conditional density estimation. *Electronic Journal of Statistics*, 11(2):2800–2831, 2017.
- Rafael Izbicki, Gilson Shimizu, and Rafael Stern. Flexible distribution-free conditional predictive bands using density estimators. In *International Conference on Artificial Intelligence and Statistics*, pages 3068–3077. PMLR, 2020.
- Rafael Izbicki, Gilson Shimizu, and Rafael B. Stern. Cd-split and hpd-split: Efficient conformal regions in high dimensions. *Journal of Machine Learning Research*, 23(87):1–32, 2022. URL <http://jmlr.org/papers/v23/20-797.html>.
- John Janowiak, Bob Joyce, and Pingping Xie. NCEP/CPC L3 half hourly 4km global (60S - 60N) merged IR v1, 2020.
- Wittawat Jitkrittum, Heishiro Kanagawa, and Bernhard Schölkopf. Testing goodness of fit of conditional density models with kernels. In Ryan P. Adams and Vibhav Gogate, editors, *Proceedings of the Thirty-Sixth Conference on Uncertainty in Artificial Intelligence, UAI 2020, virtual online, August 3-6, 2020*, volume 124 of *Proceedings of Machine Learning Research*, pages 221–230. AUAI Press, 2020a. URL <http://proceedings.mlr.press/v124/jitkrittum20a.html>.
- Wittawat Jitkrittum, Heishiro Kanagawa, and Bernhard Schölkopf. Testing goodness of fit of conditional density models with kernels. In Jonas Peters and David Sontag, editors, *Proceedings of the 36th Conference on Uncertainty in Artificial Intelligence (UAI)*, volume 124 of *Proceedings of Machine Learning Research*, pages 221–230. PMLR, 03–06 Aug 2020b. URL <http://proceedings.mlr.press/v124/jitkrittum20a.html>.
- Chris Jones and Arthur Pewsey. The sinh-arcsinh normal distribution, 2019.
- M Chris Jones and Arthur Pewsey. Sinh-arcsinh distributions. *Biometrika*, 96(4):761–780, 2009.
- Diederik P. Kingma and Jimmy Ba. Adam: A method for stochastic optimization. *arXiv preprint arXiv:1412.6980*, 2014.
- Jon Kleinberg, Sendhil Mullainathan, and Manish Raghavan. Inherent trade-offs in the fair determination of risk scores. *arXiv preprint arXiv:1609.05807*, 2016.
- Ivan Kobyzev, Simon J. D. Prince, and Marcus A. Brubaker. Normalizing flows: An introduction and review of current methods. *IEEE Trans. Pattern Anal.*

- Mach. Intell.*, 43(11):3964–3979, 2021. doi: 10.1109/TPAMI.2020.2992934. URL <https://doi.org/10.1109/TPAMI.2020.2992934>.
- Roger Koenker and Gilbert Bassett Jr. Regression quantiles. *Econometrica: Journal of the Econometric Society*, pages 33–50, 1978.
- Roger Koenker and Kevin F. Hallock. Quantile regression. *Journal of Economic Perspectives*, 15(4):143–156, 2001.
- Meelis Kull, Miquel Perelló-Nieto, Markus Kängsepp, Telmo de Menezes e Silva Filho, Hao Song, and Peter A. Flach. Beyond temperature scaling: Obtaining well-calibrated multiclass probabilities with dirichlet calibration. *CoRR*, abs/1910.12656, 2019. URL <http://arxiv.org/abs/1910.12656>.
- Christopher W. Landsea and James L. Franklin. Atlantic hurricane database uncertainty and presentation of a new database format. *Monthly Weather Review*, 141(10):3576–3592, 2013.
- Yann LeCun, Bernhard E. Boser, John S. Denker, Donnie Henderson, Richard E. Howard, Wayne E. Hubbard, and Lawrence D. Jackel. Backpropagation applied to handwritten zip code recognition. *Neural Comput.*, 1(4):541–551, 1989. doi: 10.1162/neco.1989.1.4.541. URL <https://doi.org/10.1162/neco.1989.1.4.541>.
- Jing Lei and Larry Wasserman. Distribution-free prediction bands for non-parametric regression. *Journal of the Royal Statistical Society. Series B: Statistical Methodology*, 76(1):71–96, 2014. ISSN 13697412. doi: 10.1111/rssb.12021.
- Jing Lei, Max G’Sell, Alessandro Rinaldo, Ryan J Tibshirani, and Larry Wasserman. Distribution-free predictive inference for regression. *Journal of the American Statistical Association*, 113(523):1094–1111, 2018.
- Boris Leistedt and David W. Hogg. Data-driven, Interpretable Photometric Redshifts Trained on Heterogeneous and Unrepresentative Data. *ApJ*, 838(1):5, March 2017. doi: 10.3847/1538-4357/aa6332.
- Hannelore Liero. Strong uniform consistency of nonparametric regression function estimates. *Probability theory and related fields*, 82(4):587–614, 1989.
- Yufeng Liu and Yichao Wu. Simultaneous multiple non-crossing quantile regression estimation using kernel constraints. *Journal of Nonparametric Statistics*, 23(2):415–437, 2011. doi: 10.1080/10485252.2010.537336. URL <https://doi.org/10.1080/10485252.2010.537336>. PMID: 22190842.
- Ilya Loshchilov and Frank Hutter. Decoupled weight decay regularization. In *7th International Conference on Learning Representations, ICLR 2019, New Orleans, LA, USA, May 6-9, 2019*. OpenReview.net, 2019. URL <https://openreview.net/forum?id=Bkg6RiCqY7>.
- Rachel Luo, Aadyot Bhatnagar, Huan Wang, Caiming Xiong, Silvio Savarese, Yu Bai, Shengjia Zhao, and Stefano Ermon. Localized calibration: Metrics and recalibration. *CoRR*, abs/2102.10809, 2021. URL <https://arxiv.org/abs/2102.10809>.
- Alex I. Malz and David W. Hogg. How to Obtain the Redshift Distribution from Probabilistic Redshift Estimates. *ApJ*, 928(2):127, April 2022. doi: 10.3847/1538-4357/ac062f.
- R. Mandelbaum, U. Seljak, C. M. Hirata, S. Bardelli, M. Bolzonella, A. Bongiorno, M. Carollo, T. Contini, C. E. Cunha, B. Garilli, A. Iovino, P. Kampczyk, J. P. Kneib, C. Knobel, D. C. Koo, F. Lamareille, O. Le Fèvre, J. F. Le Borgne, S. J. Lilly, C. Maier, V. Mainieri, M. Mignoli, J. A. Newman, P. A. Oesch, E. Perez-Montero, E. Ricciardelli, M. Scodeggio, J. Silverman, and L. Tasca. Precision photometric redshift calibration for galaxy-galaxy weak lensing. *MNRAS*, 386(2):781–806, May 2008. doi: 10.1111/j.1365-2966.2008.12947.x.
- Trey McNeely, Ann B. Lee, Kimberly M. Wood, and Dorit Hammerling. Unlocking GOES: A statistical framework for quantifying the evolution of convective structure in tropical cyclones. *Journal of Applied Meteorology and Climatology*, 59(10):1671–1689, 2020.
- Trey McNeely, Galen Vincent, Ann B. Lee, Rafael Izbicki, and Kimberly M. Wood. Detecting Distributional Differences in Labeled Sequence Data with Application to Tropical Cyclone Satellite Imagery. *arXiv preprint arXiv:2202.02253*, 2022.
- Mehdi Mirza and Simon Osindero. Conditional generative adversarial nets. *CoRR*, abs/1411.1784, 2014. URL <http://arxiv.org/abs/1411.1784>.
- M. J. Moreira. A conditional likelihood ratio test for structural models. *Econometrica*, 71(4):1027 – 1048, 2003.
- Mahdi Pakdaman Naeini, Gregory Cooper, and Milos Hauskrecht. Obtaining well calibrated probabilities using bayesian binning. In *Twenty-Ninth AAAI Conference on Artificial Intelligence*, 2015.
- George Papamakarios, Eric Nalisnick, Danilo Jimenez Rezende, Shakir Mohamed, and Balaji Lakshminarayanan. Normalizing Flows for Probabilistic Modeling and Inference. *arXiv e-prints*, art. arXiv:1912.02762, December 2019.
- George Papamakarios, Eric Nalisnick, Danilo Jimenez Rezende, Shakir Mohamed, and Balaji Lakshminarayanan. Normalizing flows for probabilistic modeling and inference, 2019.
- Adam Paszke, Sam Gross, Francisco Massa, Adam Lerer, James Bradbury, Gregory Chanan, Trevor Killeen, Zeming Lin, Natalia Gimelshein, Luca Antiga, Alban Desmaison, Andreas Kopf, Edward Yang, Zachary DeVito, Martin Raison, Alykhan Tejani, Sasank Chilamkurthy, Benoit Steiner, Lu Fang,

- Junjie Bai, and Soumith Chintala. Pytorch: An imperative style, high-performance deep learning library. In H. Wallach, H. Larochelle, A. Beygelzimer, F. d'Alché-Buc, E. Fox, and R. Garnett, editors, *Advances in Neural Information Processing Systems 32*, pages 8024–8035. Curran Associates, Inc., 2019. URL <http://papers.neurips.cc/paper/9015-pytorch-an-imperative-style-high-performance-deep-learning-library.pdf>.
- Yaniv Romano, Evan Patterson, and Emmanuel Candès. Conformalized quantile regression. In *Advances in Neural Information Processing Systems*, volume 32, pages 3543–3553. Curran Associates, Inc., 2019.
- I. Sadeh, F. B. Abdalla, and O. Lahav. ANNz2: Photometric Redshift and Probability Distribution Function Estimation using Machine Learning. *PASP*, 128(968):104502, October 2016. doi: 10.1088/1538-3873/128/968/104502.
- Elizabeth R. Sanabia, Bradford S. Barrett, and Caitlin M. Fine. Relationships between tropical cyclone intensity and eyewall structure as determined by radial profiles of inner-core infrared brightness temperature. *Monthly Weather Review*, 142(12):4581–4599, 2014.
- S. J. Schmidt, A. I. Malz, J. Y. H. Soo, I. A. Almosallam, M. Brescia, S. Caviuoti, J. Cohen-Tanugi, A. J. Connolly, J. DeRose, P. E. Freeman, M. L. Graham, K. G. Iyer, M. J. Jarvis, J. B. Kalmbach, E. Kovacs, A. B. Lee, G. Longo, C. B. Morrison, J. A. Newman, E. Nourbakhsh, E. Nuss, T. Pospisil, H. Tranin, R. H. Wechsler, R. Zhou, R. Izbicki, and LSST Dark Energy Science Collaboration. Evaluation of probabilistic photometric redshift estimation approaches for The Rubin Observatory Legacy Survey of Space and Time (LSST). *MNRAS*, 499(2):1587–1606, December 2020. doi: 10.1093/mnras/staa2799.
- S. J. Schmidt, A. I. Malz, J. Y. H. Soo, I. A. Almosallam, M. Brescia, S. Caviuoti, J. Cohen-Tanugi, et al. Evaluation of probabilistic photometric redshift estimation approaches for The Rubin Observatory Legacy Survey of Space and Time (LSST). *Monthly Notices of the Royal Astronomical Society*, 499(2):1587–1606, 2020.
- W. Stute and L. X. Zhu. Model checks for generalized linear models. *Scandinavian Journal of Statistics*, 29(3):535 – 545, 2002. ISSN 0303-6896.
- Natasa Tagasovska and David Lopez-Paz. Single-model uncertainties for deep learning. In Hanna M. Wallach, Hugo Larochelle, Alina Beygelzimer, Florence d'Alché-Buc, Emily B. Fox, and Roman Garnett, editors, *Advances in Neural Information Processing Systems 32: Annual Conference on Neural Information Processing Systems 2019, NeurIPS 2019, December 8-14, 2019, Vancouver, BC, Canada*, pages 6414–6425, 2019. URL <https://proceedings.neurips.cc/paper/2019/hash/73c03186765e199c116224b68adc5fa0-Abstract.html>.
- Sean Talts, Michael Betancourt, Daniel Simpson, Aki Vehtari, and Andrew Gelman. Validating bayesian inference algorithms with simulation-based calibration. *arXiv preprint arXiv:1804.06788*, 2018.
- James W Taylor and Derek W Bunn. A quantile regression approach to generating prediction intervals. *Management Science*, 45(2):225–237, 1999.
- Allan Timmermann. Density forecasting in economics and finance. *Journal of Forecasting*, 19(4):231, 2000.
- Aäron van den Oord and Nal Kalchbrenner. Pixel RNN. 2016.
- Aaron Van den Oord, Nal Kalchbrenner, Lasse Espeholt, Oriol Vinyals, Alex Graves, et al. Conditional image generation with pixelcnn decoders. *Advances in neural information processing systems*, 29, 2016.
- Vladimir Vovk, Alex Gammerman, and Glenn Shafer. *Algorithmic Learning in a Random World*. Springer Science & Business Media, 2005. ISBN 0-387-00152-2.
- Yoav Wald and Amir Globerson. Robust conditional probabilities. In Isabelle Guyon, Ulrike von Luxburg, Samy Bengio, Hanna M. Wallach, Rob Fergus, S. V. N. Vishwanathan, and Roman Garnett, editors, *Advances in Neural Information Processing Systems 30: Annual Conference on Neural Information Processing Systems 2017, December 4-9, 2017, Long Beach, CA, USA*, pages 6359–6368, 2017. URL <https://proceedings.neurips.cc/paper/2017/hash/3eb414bflc2a66a09c185d60553417b8-Abstract.html>.
- Antoine Wehenkel and Gilles Louppe. Unconstrained monotonic neural networks. In Hanna M. Wallach, Hugo Larochelle, Alina Beygelzimer, Florence d'Alché-Buc, Emily B. Fox, and Roman Garnett, editors, *Advances in Neural Information Processing Systems 32: Annual Conference on Neural Information Processing Systems 2019, NeurIPS 2019, December 8-14, 2019, Vancouver, BC, Canada*, pages 1543–1553, 2019. URL <https://proceedings.neurips.cc/paper/2019/hash/2a084e55c87b1ebcdaad1f62fdbbac8e-Abstract.html>.
- David Zhao, Niccolò Dalmaso, Rafael Izbicki, and Ann B. Lee. Diagnostics for conditional density models and bayesian inference algorithms. In Cassio de Campos and Marloes H. Maathuis, editors, *Proceedings of the Thirty-Seventh Conference on Uncertainty in Artificial Intelligence*, volume 161 of *Proceedings of Machine Learning Research*, pages 1830–1840. PMLR, 27–30 Jul 2021. URL <https://proceedings.mlr.press/v161/zhao21b.html>.
- Shengjia Zhao, Tengyu Ma, and Stefano Ermon. Individual calibration with randomized forecasting. In *International*

Conference on Machine Learning, pages 11387–11397.
PMLR, 2020.

Rongpu Zhou, Jeffrey A. Newman, Yao-Yuan Mao, Aaron Meisner, John Moustakas, Adam D. Myers, Abhishek Prakash, Andrew R. Zentner, David Brooks, Yutong Duan, Martin Landriau, Michael E. Levi, Francisco Prada, and Gregory Tarle. The clustering of DESI-like luminous red galaxies using photometric redshifts. *MNRAS*, 501(3):3309–3331, March 2021. doi: 10.1093/mnras/staa3764.

A Cal-PIT (HPD) and Cal-HPD

Cal-PIT (HPD) Cal-PIT can also be used to compute Highest Predictive Density regions (HPDs) instead of prediction intervals. The oracle $(1-\alpha)$ -level HPD set is defined as

$$\text{HPD}_\alpha(\mathbf{x}) = \{y : f(y|\mathbf{x}) \geq t_{\mathbf{x},\alpha}\},$$

where $t_{\mathbf{x},\alpha}$ is such that $\int_{y \in \text{HPD}_\alpha(\mathbf{x})} f(y|\mathbf{x}) dy = 1 - \alpha$. HPDs are the smallest prediction sets that have coverage $1 - \alpha$, and thus they may be more precise (smaller set size) than quantile-based intervals, while maintaining the conditional coverage at the nominal level (see Appendix D for an example with a bimodal predictive distribution).

The Cal-PIT estimate of $\text{HPD}_\alpha(\mathbf{x})$ is given by

$$C_\alpha(\mathbf{x}) = \{y : \tilde{f}(y|\mathbf{x}) \geq \tilde{t}_{\mathbf{x},\alpha}\},$$

where $\tilde{t}_{\mathbf{x},\alpha}$ is such that $\int_{y \in C_\alpha(\mathbf{x})} \tilde{f}(y|\mathbf{x}) dy = 1 - \alpha$ and \tilde{f} is the Cal-PIT calibrated CDE (Algorithm 1).

Remark 2 (cal-HPD). *Alternatively, one can directly use HPD values, defined as*

$$\hat{H}(y; \mathbf{x}) := \int_{\{y' : \hat{f}(y'|\mathbf{x}) \leq \hat{f}(y|\mathbf{x})\}} \hat{f}(y'|\mathbf{x}) dy',$$

to recalibrate HPD prediction sets (rather than using PIT values). The idea is to estimate the local HPD coverage at each \mathbf{x} , $h^{\hat{f}}(\gamma; \mathbf{x}) := \mathbb{P}(\hat{H}(Y; \mathbf{x}) \leq \gamma | \mathbf{x})$, by regression, analogous to estimating the PIT-CDF in Cal-PIT. Let $\hat{h}^{\hat{f}}(\gamma; \mathbf{x})$ be such an estimate. The recalibrated $(1-\alpha)$ -level HPD set at a location \mathbf{x} is given by the $(1-\alpha^(\mathbf{x}))$ -level HPD set of the original density $\hat{f}(y|\mathbf{x})$, where $\alpha^*(\mathbf{x})$ is such that $\hat{h}^{\hat{f}}(\alpha^*(\mathbf{x}); \mathbf{x}) = \alpha$. This framework however does not yield full PDs. Moreover, although the approach corrects HPD sets, aiming for conditional coverage, the constructed sets will not be optimal if the initial model \hat{f} is misspecified.*

In this work, we only report results for Cal-PIT(INT) and Cal-PIT(HPD); we do not report results for Cal-HPD.

B Algorithm for Cal-PIT

Algorithm 1 Cal-PIT

Require: initial CDE $\hat{f}(y|\mathbf{x})$; calibration set $\mathcal{D} = \{(\mathbf{x}_1, y_1), \dots, (\mathbf{x}_n, y_n)\}$; oversampling factor K ; test points $\mathcal{V} = \{\mathbf{x}_1, \dots, \mathbf{x}_m\}$; grid G of values $\gamma \in (0, 1)$ for evaluating PIT-CDF after training; nominal miscoverage level α , flag HPD (true if computing HPD sets)

Ensure: calibrated CDF $\tilde{F}(y|\mathbf{x})$, Cal-PIT interval $C(\mathbf{x})$, calibrated CDE $\tilde{f}(y|\mathbf{x})$, for all $\mathbf{x} \in \mathcal{V}$

```

1: // Learn PIT-CDF from augmented and upsampled
   calibration data  $\mathcal{D}'$ 
2: Set  $\mathcal{D}' \leftarrow \emptyset$ 
3: for  $i$  in  $\{1, \dots, n\}$  do
4:   for  $j$  in  $\{1, \dots, K\}$  do
5:     Draw  $\gamma_{i,j} \sim U(0, 1)$ 
6:     Compute  $W_{i,j} \leftarrow \mathbb{I}(\text{PIT}(Y_i; \mathbf{X}_i) \leq \gamma_{i,j})$ 
7:     Let  $\mathcal{D}' \leftarrow \mathcal{D}' \cup \{(\mathbf{X}_i, Y_i, W_{i,j})\}$ 
8:   end for
9: end for
10: Use  $\mathcal{D}'$  to learn  $\hat{r}^{\hat{f}}(\gamma; \mathbf{x}) := \hat{\mathbb{P}}(\text{PIT}(Y; \mathbf{x}) \leq \gamma | \mathbf{x})$  via
    a regression of  $W$  on  $\mathbf{X}$  and  $\gamma$ , which is monotonic w.r.t.
     $\gamma$ .
11:
12: // Calibration using PIT-CDF
13: for  $\mathbf{x} \in \mathcal{V}$  do
14:   Set  $\mathcal{S} \leftarrow \emptyset$ 
15:   for  $\gamma \in G$  do
16:     Compute  $\beta \leftarrow \hat{r}^{\hat{f}}(\gamma; \mathbf{x})$ 
17:     Let  $\tilde{F}^{-1}(\beta|\mathbf{x}) \leftarrow \tilde{F}^{-1}(\gamma|\mathbf{x})$ 
18:      $\mathcal{S} \leftarrow \mathcal{S} \cup \{(\tilde{F}^{-1}(\gamma|\mathbf{x}), \beta)\}$ 
19:   end for
20:   Apply interpolating (or smoothing) splines to  $\mathcal{S}$  to
    obtain  $\tilde{F}(\cdot|\mathbf{x})$  and  $\tilde{F}^{-1}(\cdot|\mathbf{x})$ 
21:   // Construct Cal-PIT interval with conditional
    coverage  $1 - \alpha$ 
22:   Compute  $C(\mathbf{x}) \leftarrow [\tilde{F}^{-1}(0.5\alpha|\mathbf{x}); \tilde{F}^{-1}(1 - 0.5\alpha|\mathbf{x})]$ .
23:   // Construct recalibrated CDF and CDE
24:   Evaluate  $\tilde{F}(y|\mathbf{x})$  at the same  $y$ -values as the initial
    CDE  $\hat{f}(y|\mathbf{x})$ 
25:   Differentiate  $\tilde{F}(y|\mathbf{x})$  to obtain recalibrated PDF
     $\tilde{f}(y|\mathbf{x})$ 
26:   Renormalize  $\tilde{f}(y|\mathbf{x})$  according to Izbicki and Lee
    [2016, Section 2.2]
27:   if HPD then
28:     Obtain HPD sets  $C(\mathbf{x}) = \{y : \tilde{f}(y|\mathbf{x}) \geq \tilde{t}_{\mathbf{x},\alpha}\}$ ,
    where  $\tilde{t}_{\mathbf{x},\alpha}$  is such that  $\int_{y \in C_\alpha(\mathbf{x})} \tilde{f}(y|\mathbf{x}) dy = 1 - \alpha$ 
29:   end if
30: end for
31: return  $\tilde{F}(y|\mathbf{x})$ ,  $C(\mathbf{x})$ ,  $\tilde{f}(y|\mathbf{x})$ , for all  $\mathbf{x} \in \mathcal{V}$ 

```

C Proofs

Lemma 1. *Let G and H be two cumulative distribution functions such that G dominates H , and let μ_G and μ_H be their associated measures over \mathbb{R} . Then, for every fixed $y \in \mathbb{R}$,*

$$\mu_H(\{y' \in \mathbb{R} : y' \leq y\}) = \mu_H(\{y' \in \mathbb{R} : G(y') \leq G(y)\}).$$

Proof. Fix $y \in \mathbb{R}$ and let $A = \{y' \in \mathbb{R} : y' \leq y\}$ and $B = \{y' \in \mathbb{R} : G(y') \leq G(y)\}$. Because $A \subseteq B$,

$$\mu_H(A) \leq \mu_H(B). \quad (7)$$

We note that $\mu_G(B \cap A^c) = 0$. From this and the assumption that G dominates H , we conclude that $\mu_H(B \cap A^c) = 0$. It follows that

$$\begin{aligned} \mu_H(B) &= \mu_H(B \cap A) + \mu_H(B \cap A^c) \leq \mu_H(A) + 0 \\ &= \mu_H(A). \end{aligned} \quad (8)$$

From Equations 7 and 8, we conclude that $\mu_H(A) = \mu_H(B)$. \square

Lemma 2. *Fix $y \in \mathbb{R}$ and let $\gamma := \hat{F}(y|\mathbf{x})$. Then, under Assumptions 1 and 2, $\tilde{F}(y|\mathbf{x}) = \hat{r}^{\hat{F}}(\gamma; \mathbf{x})$ and $F(y|\mathbf{x}) = r^{\hat{F}}(\gamma; \mathbf{x})$.*

Proof. We note that $\gamma = \hat{F}(y|\mathbf{x})$ implies that $y = \hat{F}^{-1}(\gamma|\mathbf{x})$. It follows then by construction,

$$\tilde{F}(y|\mathbf{x}) = \tilde{F}(\hat{F}^{-1}(\gamma|\mathbf{x})|\mathbf{x}) = \hat{r}^{\hat{F}}(\gamma; \mathbf{x}).$$

Moreover,

$$F(y|\mathbf{x}) = \mathbb{P}(Y \leq y|\mathbf{x}) \quad (9)$$

$$\begin{aligned} &= \mathbb{P}(\hat{F}(Y|\mathbf{x}) \leq \hat{F}(y|\mathbf{x})|\mathbf{x}) \\ &\quad (\text{Assumption 2 and Lemma 1}) \\ &= \mathbb{P}(\text{PIT}(Y; \mathbf{x}) \leq \hat{F}(y|\mathbf{x})|\mathbf{x}) \end{aligned} \quad (10)$$

$$\begin{aligned} &= \mathbb{P}(\text{PIT}(Y; \mathbf{x}) \leq \gamma|\mathbf{x}) \\ &= r^{\hat{F}}(\gamma; \mathbf{x}), \end{aligned} \quad (11)$$

which concludes the proof. \square

Proof of Theorem 1. Consider the change of variables $\gamma = \hat{F}(y|\mathbf{x})$, so that $d\gamma = \hat{f}(y|\mathbf{x})dy$. Lemma 2 implies that $\tilde{F}(y|\mathbf{x}) = \hat{r}^{\hat{F}}(\gamma; \mathbf{x})$ and $F(y|\mathbf{x}) = r^{\hat{F}}(\gamma; \mathbf{x})$. It follows from that and Assumption 3 that

$$\begin{aligned} &\int \int (\tilde{F}(y|\mathbf{x}) - F(y|\mathbf{x}))^2 dP(y, \mathbf{x}) \\ &\leq K \int \int (\tilde{F}(y|\mathbf{x}) - F(y|\mathbf{x}))^2 \hat{f}(y|\mathbf{x}) dy P(\mathbf{x}) \\ &= K \int \int (\hat{r}^{\hat{F}}(\gamma; \mathbf{x}) - r^{\hat{F}}(\gamma; \mathbf{x}))^2 d\gamma dP(\mathbf{x}). \end{aligned}$$

The conclusion follows from Assumption 4. \square

Proof of Theorem 2. From Lemma 2,

$$\begin{aligned} &\sup_{\mathbf{x} \in \mathcal{X}, y \in \mathbb{R}} |\tilde{F}(y|\mathbf{x}) - F(y|\mathbf{x})| \\ &= \sup_{\mathbf{x} \in \mathcal{X}, \gamma \in [0,1]} |\hat{r}^{\hat{F}}(\gamma; \mathbf{x}) - r^{\hat{F}}(\gamma; \mathbf{x})| \xrightarrow[n \rightarrow \infty]{\text{a.s.}} 0, \end{aligned}$$

where the last step follows from Assumption 5. It then follows from Assumption 1 that

$$\sup_{\mathbf{x} \in \mathcal{X}, \gamma \in [0,1]} |\tilde{F}^{-1}(\gamma|\mathbf{x}) - F^{-1}(\gamma|\mathbf{x})| \xrightarrow[n \rightarrow \infty]{\text{a.s.}} 0,$$

and, in particular,

$$\sup_{\mathbf{x} \in \mathcal{X}, \alpha \in \{.5\alpha, 1-.5\alpha\}} |\tilde{F}^{-1}(\alpha|\mathbf{x}) - F^{-1}(\alpha|\mathbf{x})| \xrightarrow[n \rightarrow \infty]{\text{a.s.}} 0,$$

from which the conclusion of the theorem follows. \square

C.1 Theory for Cal-PIT HPD sets

For every $\mathbf{x} \in \mathcal{X}$, let $C_\alpha(\mathbf{x}) = \{y : \tilde{f}(y|\mathbf{x}) \geq \tilde{t}_{\mathbf{x},\alpha}\}$, where $\tilde{t}_{\mathbf{x},\alpha}$ is such that $\int_{y \in C_\alpha(\mathbf{x})} \tilde{f}(y|\mathbf{x}) dy = 1 - \alpha$ be the Cal-PIT HPD-set. Similarly, let $\text{HPD}_\alpha(\mathbf{x}) = \{y : f(y|\mathbf{x}) \geq t_{\mathbf{x},\alpha}\}$, where $t_{\mathbf{x},\alpha}$ is such that $\int_{y \in \text{HPD}_\alpha(\mathbf{x})} f(y|\mathbf{x}) dy = 1 - \alpha$ be the true HPD-set. The next theorem shows that if the probabilistic classifier is well estimated, then Cal-PIT HPD sets are exactly equivalent to oracle HPD sets.

Theorem 3 (Fisher consistency Cal-PIT HPD-sets). *Fix $\mathbf{x} \in \mathcal{X}$. If $\hat{r}(\gamma; \mathbf{x}) = r(\gamma; \mathbf{x})$ for every $\gamma \in [0, 1]$, $C_\alpha(\mathbf{x}) = \text{HPD}_\alpha(\mathbf{x})$ and $\mathbb{P}(Y \in C_\alpha(\mathbf{X})|\mathbf{x}) = 1 - \alpha$.*

Proof of Theorem 3. Fix $y \in \mathbb{R}$ and let $\gamma = \hat{F}(y|\mathbf{x})$, so that $y = \hat{F}^{-1}(\gamma|\mathbf{x})$. It follows that

$$\begin{aligned} \tilde{F}(y|\mathbf{x}) &= \tilde{F}(\hat{F}^{-1}(\gamma|\mathbf{x})|\mathbf{x}) = \hat{r}(\gamma; \mathbf{x}) = r(\gamma; \mathbf{x}) \\ &= \mathbb{P}(\hat{F}(Y|\mathbf{x}) \leq \hat{F}(y|\mathbf{x})|\mathbf{x}, \gamma) = \mathbb{P}(Y \leq y|\mathbf{x}, \gamma) \\ &= F(y|\mathbf{x}), \end{aligned}$$

and therefore $\tilde{f}(y|\mathbf{x}) = f(y|\mathbf{x})$ for almost every $y \in \mathbb{R}$. It follows that $C_\alpha(\mathbf{x}) = \text{HPD}_\alpha(\mathbf{x})$. The claim about conditional coverage follows from the definition of the HPD. \square

D Examples 1 and 2

Example 1

The data for Example 1 (Section 4.1) consist of two groups with different spreads:

$$\begin{aligned} \epsilon_1 &\sim N(0, 1), \epsilon_2 \sim N(0, 0.1^2), \\ X_0 &\sim \text{Bern}(0.2), X_{1,2} \stackrel{\text{i.i.d.}}{\sim} \text{Unif}[-5, 5]^2, \\ Y &= \begin{cases} 3\epsilon_2 + 0.2(X_1 + 5)\epsilon_1, & X_0 = 0, X_1 < 0 \\ 3\epsilon_2 - 0.2(X_1 - 5)\epsilon_1, & X_0 = 1, X_1 < 0 \\ 3\epsilon_2 + 0.2(X_1 + 5)\epsilon_1 + X_1, & X_0 = 0, X_1 > 0 \\ 3\epsilon_2 - 0.2(X_1 - 5)\epsilon_1 - X_1, & X_0 = 1, X_1 > 0 \end{cases} \end{aligned}$$

Figure 8 shows that both Cal-PIT (INT) and Cal-PIT (HPD) have set sizes that are as small as their optimal counterparts (“Oracle Band” and “Oracle HPD”, respectively), and that Cal-PIT (HPD) sets are indeed more informative (that is, the regions are smaller) than Cal-PIT (INT) .

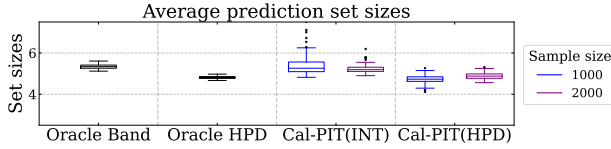


Figure 8: Average prediction set sizes for test points for different methods along with the ideal “Oracle Band” and “Oracle HPD”. Box plots show the size distribution for multiple trials of the experiment. Cal-PIT achieves prediction sets that are at least as tight as those by other methods, while simultaneously providing more accurate coverage.

We saw that this example is difficult for both quantile regression (QR) and orthogonal quantile regression (OQR) to learn (see Figure 2). OQR augments the standard pinball loss of QR with a penalty on the correlation between prediction set size and coverage, which can improve conditional coverage in certain settings [Feldman et al., 2021], but is not very helpful in this example. Figure 9 shows that the initial prediction sets learned by QR have bad conditional coverage, but also do not have much correlation between size and coverage. Thus, the penalty applied by OQR is unable to substantially improve upon the QR results.

We emphasize that methods like OQR target *proxies* for conditional coverage, while our Cal-PIT method *directly* targets conditional coverage. Therefore, our method succeeds in more general settings. Example 1 is a case where penalizing the correlation between prediction set size and coverage is not a good proxy for achieving conditional coverage, so OQR is not as successful as Cal-PIT at achieving conditional coverage.

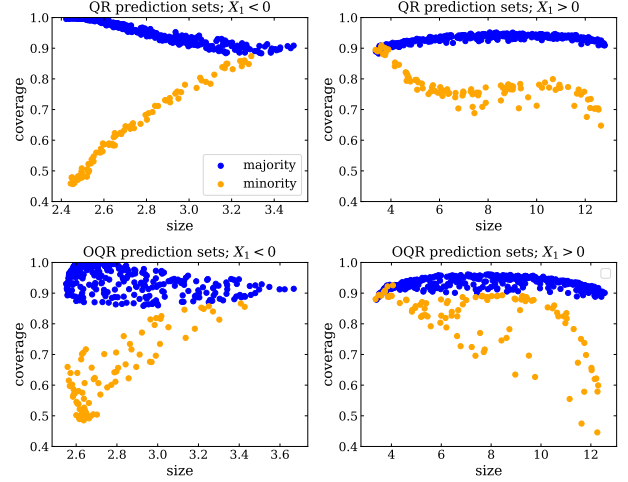


Figure 9: *Top*: Prediction sets from quantile regression (QR). We see clear correlations between size and coverage, but note that X_0 is not actually available as a predictor, i.e. we cannot “see” the blue and orange colors. The overall correlations, without the colors, are weak. *Bottom*: Prediction sets from orthogonalized quantile regression (OQR). Because the overall correlation between size and coverage is weak, penalizing it does not change the results very much. In particular, we still see high correlations (and bad conditional coverage) in the minority group.

Example 2

For Example 2 (Section 4.2), the training distribution is Gaussian,

$$Y_0|X \sim \mathcal{N}(\mu = X, \sigma = 2),$$

while the two target distributions have skew and kurtosis:

$$\begin{aligned} Y_1|X &\sim \sinh\text{-arcsinh}(\mu = X, \sigma = 2 - |X|, \gamma = X, \tau = 1), \\ Y_2|X &\sim \sinh\text{-arcsinh}(\mu = X, \sigma = 2, \gamma = 0, \tau = 1 - X/4). \end{aligned}$$

The family of $\sinh\text{-arcsinh}$ normal distributions [Jones and Pewsey, 2009, 2019] has been suggested before by Barnes et al. [2021] as a flexible parametric model that supports estimation of the type of heteroscedastic, asymmetric uncertainties often observed in climate data.

E Photometric Redshift CDEs

As described in Section 5.2, due to the noisy and limited information about redshift contained in galaxy images, galaxies with similar imaging data may have different redshifts and vice versa. We want this property to be captured in photo- z PDs, requiring them to be multimodal. As we do not know the “ground truth” CDEs, we generally have to rely on indirect methods to assess coverage. Here we provide a rudimentary but direct demonstration that the CDEs

we predict are indeed meaningful. We compare the CDEs of the five galaxies shown in Fig. 7 with the distribution of true redshifts of other galaxies with similar imaging data. We identify those counterparts by searching for other galaxies in the training set whose colors and magnitudes (rescaled by subtracting the mean and dividing by the standard deviation for each feature) lie within a Euclidean distance of 0.5 units of our selected galaxies. Fig. 10 shows their redshift distribution as an inverse-distance weighted histogram along with their CDEs. We observe that the histograms show bimodal distributions when our inferred CDEs are bimodal and unimodal when the inferred distribution is unimodal, matching expectations.

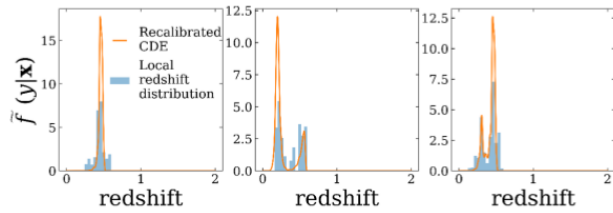


Figure 10: Comparison of photo- z CDEs for the galaxies shown in Fig. 7 with the distribution of true redshifts of other galaxies having similar imaging properties. We observe that the histograms show bimodal distributions only when our inferred CDEs are bimodal.

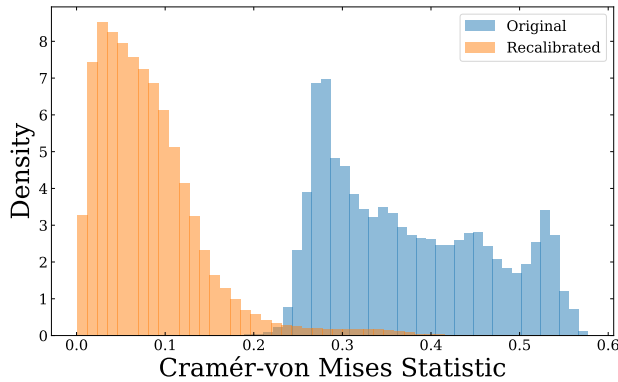


Figure 11: Distribution of the Cramér-von Mises (CvM) Statistic (i.e., mean squared difference) between the local PIT CDF of each galaxy in the test set and the CDF of a Uniform distribution. As the “ground truth” CDEs are unknown, we assess conditional coverage by training regression models to predict the local PIT CDFs on the calibration and validation sets. We observe a significant decrease in the value of CvM statistic for the entire test set, with the average value decreasing by $\sim 4.5\times$. The value of CDE loss [Izbicki and Lee, 2017] which is another independent measure of conditional coverage decreases from -0.84 to -10.71 after recalibration.

F Training a regression model to learn

$$\hat{r}^f(\gamma; \mathbf{x})$$

The success of Cal-PIT depends entirely on learning an accurate representation of $\hat{r}^f(\gamma; \mathbf{x})$. One can in principle choose any regression algorithm and pair it with 1. We use monotonic neural networks from Wehenkel and Louppe [2019] as our regression method as we find this architecture gives reasonably good results for all of our experiments. The network is constrained to be monotonic w.r.t. the coverage level (α) and uses identical sets of fully connected sub-networks to learn the monotonic dependence and the unconstrained dependence separately, with the two results merged in the final layer of the network. It is known that neural networks struggle with categorical inputs and in that case, tree-based regression methods or an additional embedding step might produce better results.

For synthetic example-1 and the photometric redshift demonstration, we use a network architecture with 3 hidden layers with 512 nodes each and for synthetic example-2 we use a network architecture with 3 hidden layers with 128 nodes each (see Section G for the details on example 3). We use the ReLU activation function Glorot et al. [2011] for all the hidden layers and the AdamW optimizer Loshchilov and Hutter [2019] with an initial learning rate of 0.001 and weight decay parameter set to 0.01. We follow a multiplicative weight decay schedule given by the rule: $\text{learning rate}(\text{epoch}) = \text{initial learning rate} \times 0.95^{\text{epoch}}$. Following assumption 4, we minimize the mean squared error to train the models. The data used to train the model is split into 90:10 partitions where 90% of the data is used to optimize the loss function and 10% of the data is used to calculate a validation mean squared error loss every epoch on a fixed grid of α . To prevent our model from over-fitting we stop training once the validation loss does not decrease for 10 epochs and save the model with the best validation loss. We use a batch size of 2048 throughout and oversample our training data by a factor (K) of 50.

We used PyTorch Paszke et al. [2019] to create and train our neural network models and trained them on a single Nvidia A100 GPU. If a value of any hyperparameter is not explicitly mentioned here in the text, it implies that we used the default values set in PyTorch. Training times for all our experiments range from a few minutes to about an hour at maximum.

G Details on Probabilistic Nowcasting Application

G.1 Tropical Cyclone Data

We use TC intensity and location data from NOAA’s HURDAT2 best track database [Landsea and Franklin, 2013], and GOES longwave infrared imagery from NOAA’s

MERGIR database [Janowiak et al., 2020]. HURDAT2 best tracks are provided at 6-hour time resolution, while the GOES IR imagery is available at a 30-minute \times 4-km resolution over both the North Atlantic (NAL) and Eastern North Pacific (ENP) basins from 2000–2020. Every thirty minutes during the lifetime of a storm, we record a ~ 800 km \times 800 km “stamp” of IR imagery surrounding the TC location, showing cloud-top temperatures for the storm. Figure 12 (left) shows two such stamps.

The radial profile, defined as $T(r) = \frac{1}{2\pi} \int_0^{2\pi} T_b(r, \theta) d\theta$, captures the structure of cloud-top temperatures T_b as a function of radius r from the TC center and serves as an easily interpretable description of the depth and location of convection near the TC core [McNeely et al., 2020, Sanabia et al., 2014]. The radial profiles are computed at 5-km resolution from 0–400km ($d = 80$) (Figure 12, center). Finally, at each time t we stack the preceding 24 hours (48 profiles) into a structural trajectory, $\mathbf{S}_{<t}$, consisting of an image of the most recent 48 rows of the data. We visualize these summaries over time with Hovmöller diagrams (Hovmöller [1949]; see Figure 12, right).

Figure 13 shows an example sequence of observed radial profiles every 30 minutes for a real TC, along with observed wind speed Y . We interpolate Y , which is available every 6 hours, to a 30-minute resolution.

Our goal is to create a synthetic example that has a similar dependency structure as actual TCs.

G.2 Synthetic Model for High-Dimensional Sequence Data

Using the radial profiles from all TC data, we perform a principal component analysis (PCA). Figure 14 shows the first three principal components, or empirical orthogonal functions (EOFs). Figure 13 shows the observation and reconstruction of the TC using just these three EOFs. To create the synthetic data in Example 3, we use a similar reconstruction scheme:

Let $\Delta PC_t := PC_t - PC_{t-30m}$ be the 30-minute change in a PC coefficient at time t for observed data. We fit a vector autoregression (VAR) model to $(\Delta PC1_t, \Delta PC2_t, \Delta PC3_t)$ to capture the dependence of each component on its own lags as well as the lags of the other components. The model chosen by the BIC criterion has order 3, for a lag of 90 minutes.

With the fitted VAR model, we can jointly simulate synthetic time series data for $PC1, PC2, PC3$. A TC structural trajectory is constructed by multiplying simulated time series of PCA coefficients with their corresponding eigenvectors (Figure 14).

G.3 Synthetic Model for Intensities

To model the time evolution of intensities Y , we fit a time series regression of intensity change on its past values together with PC coefficients for present and past TC structure.

Let $Z := \text{logit}(Y/200)$ so that simulated values of intensities Y are reasonable, i.e. fall between 0 and 200. We then define $\Delta Z_t = Z_t - Z_{t-6h}$. Finally, we fit the following linear regression model for ΔZ :

$$\begin{aligned} \Delta Z_t = & \beta_0 + \beta_1 Z_{t-6h} + \beta_2 \Delta Z_{t-6h} + \beta_3 PC1_t \\ & + \beta_4 PC2_t + \beta_5 PC3_t + \beta_6 PC1_{t-6h} \\ & + \beta_7 PC2_{t-6h} + \beta_8 PC3_{t-6h} + \beta_9 PC1_{t-12h} \\ & + \beta_{10} PC2_{t-12h} + \beta_{11} PC3_{t-18h} \\ & + \beta_{12} PC2_{t-24h} + \epsilon_t \end{aligned}$$

where ϵ_t is Gaussian noise with mean 0 and standard deviation set to the root mean squared error between the real and predicted radial profiles in the training set. Note that ΔZ_t has dependencies on its own lagged values as well as lagged values of PC_t .

Figure 5 in Section 5.1 shows an example TC with simulated radial profiles that update every 30 minutes, with accompanying simulated wind speed Y every 30 minutes.

As a sanity check, we check that the marginal distributions of the simulated and real wind speed values (Y) look similar, as shown in Figure 15.

G.4 Re-calibration of Convolutional MDN Results of Intensity Distribution

With our trained VAR model, we generate a very long time series for $PC1, PC2, PC3$ with a value of the PC ’s randomly selected from the training set of storms as the initial point. The time series is then divided into 24-hour-long chunks and the structural trajectory and intensities are reconstructed. We create 8000 such instances for our training set, 8000 more for our calibration set, and 4000 instances for our test sets. We rejected a 24-hour long window between each chunk of the time series to ensure that each instance has no memory of the previous ones.

We fit a unimodal Gaussian neural density model to estimate the conditional density $f(y|s)$ of TC intensities given past radial profiles. Specifically, we fit a convolutional mixture density network (ConvMDN, D’Isanto and Polsterer [2018]) with a single Gaussian component, two convolutional and two fully connected layers which gives an initial estimate of $f(y|s)$.

We then use a convolutional neural network LeCun et al. [1989], Fukushima and Miyake [1982] model with two

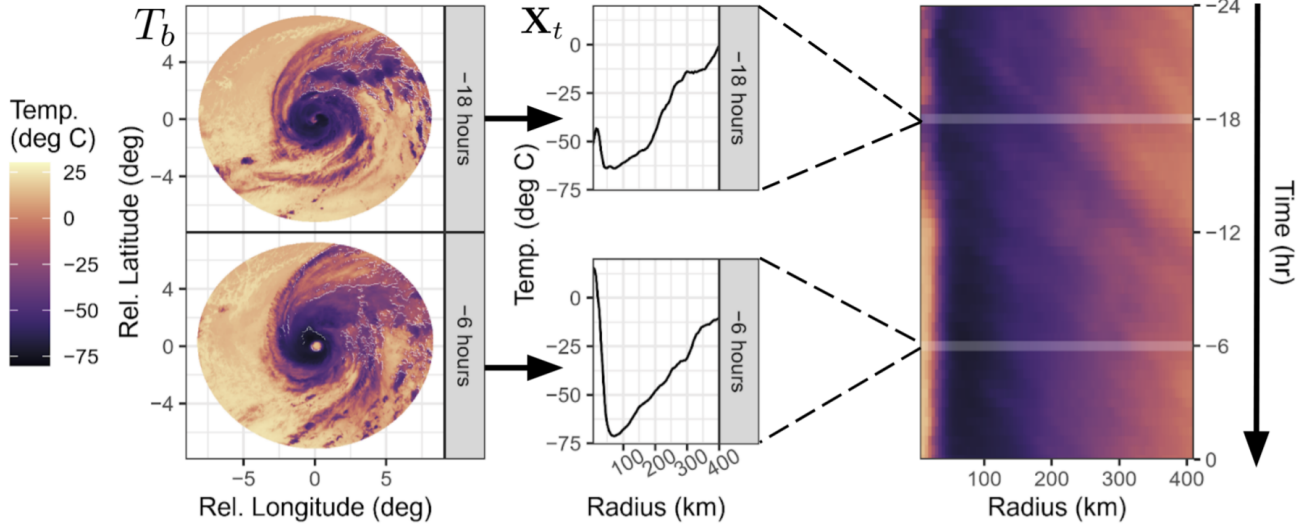


Figure 12: *Left*: The raw data is a sequence of TC-centered cloud-top temperature images from GOES. *Center*: We convert each GOES image into a radial profile. *Right*: The 24-hour sequence of consecutive radial profiles, sampled every 30 minutes, defines a structural trajectory or Hovmöller diagram. These trajectories serve as high-dimensional inputs for predicting TC intensity. Figure from [McNeely et al., 2022].

convolutional layers followed by 5 fully connected layers which take the structural trajectory images and the coverage level (α) as inputs training. The network output is restricted to be monotonic w.r.t. α Wehenkel and Louppe [2019]. For both the models we use ReLU activations [Glorot et al., 2011] for intermediate layers and train using the Adam optimizer [Kingma and Ba, 2014] with learning rate 10^{-3} , $\beta_1 = 0.9$, and $\beta_2 = 0.999$. We use the same multiplicative learning rate decay schedule mentioned in F.

G.5 Additional Example 3 Results

The ConvMDN struggles in this example because of the conditional distribution of $Y|S$ sometimes being skewed towards larger intensities; this phenomenon can partly be observed in Figure 16, where we show the distribution of Y_t at fixed values of t for some example simulated TCs. Cal-PIT is able to adjust for the model misspecification (similar to Example 2), resulting in narrower prediction bands that are still conditionally valid. Figure 17 shows a few more examples of prediction sets for simulated TCs before and after calibration.

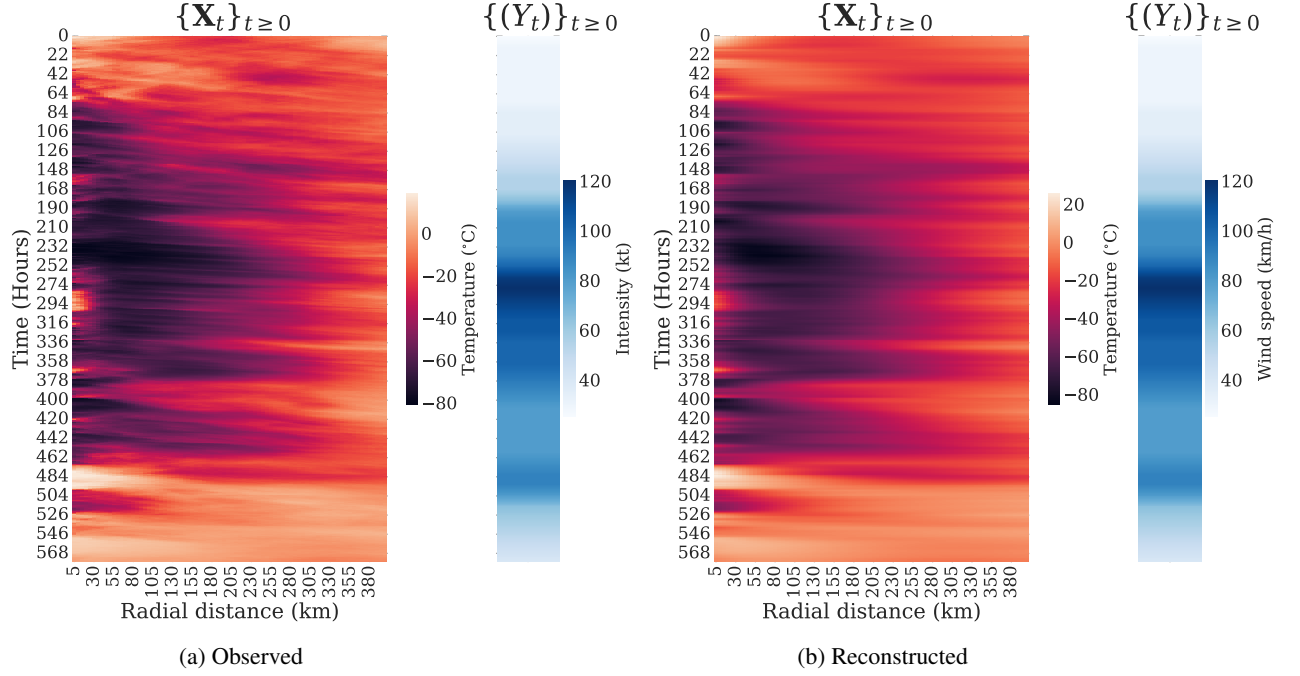


Figure 13: Observed and reconstructed radial profiles X_t over time for Hurricane Teddy 2020 (*left*). These are recorded every 30 mins. We obtain a decent reconstruction by using the first 3 PCs. Observed wind speed values Y_t , recorded every 6 hours but interpolated on the same 30 min grid (*right*).

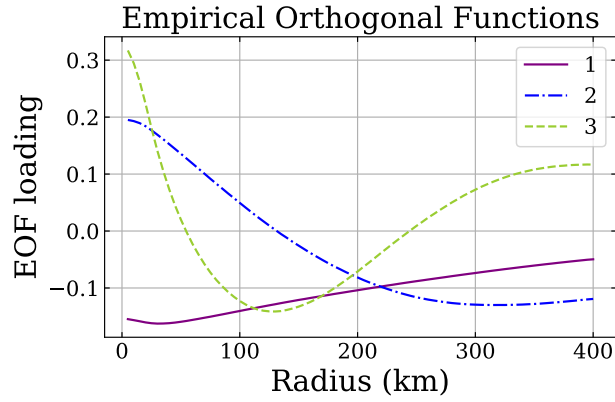


Figure 14: Top 3 PCA components, or empirical orthogonal functions (EOFs), for TC radial profiles.

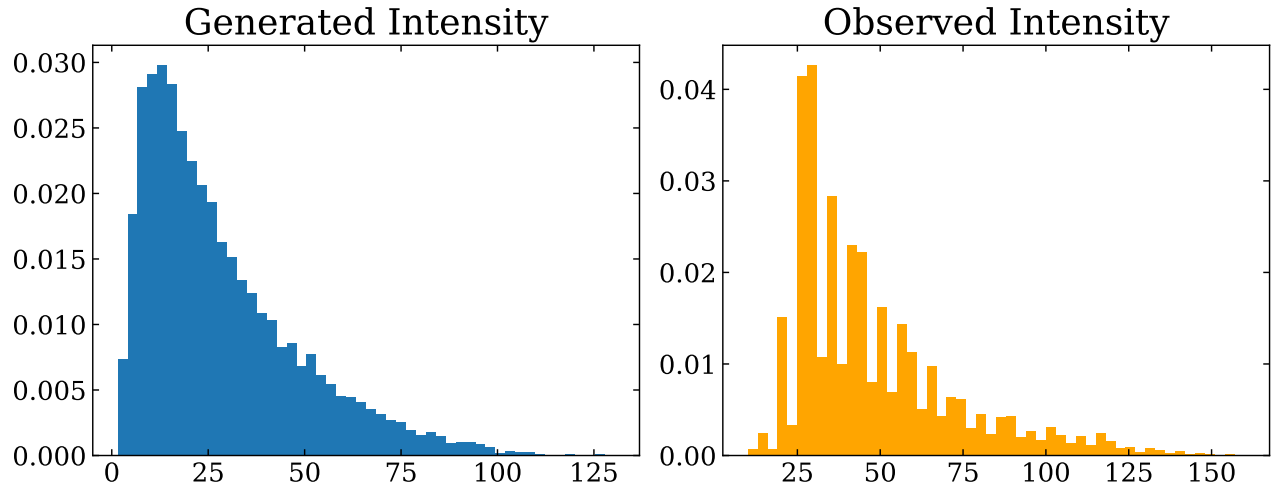


Figure 15: *Left*: Marginal distribution of generated wind speed values Y , based on the model in Equation 12. *Right*: Marginal distribution of observed wind speed values.

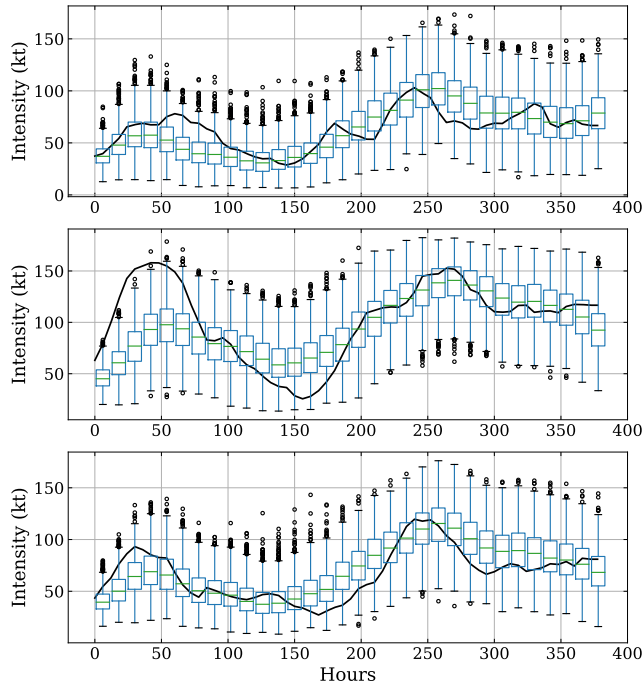


Figure 16: Boxplots of the distribution of Y_t at fixed values of t , for simulated TCs. The distributions show skewness, which may explain why the uncalibrated ConvMDN does not fit perfectly. Moreover, the calibrated prediction sets appear to track the observed trajectories (black curves) more closely than the ConvMDN.

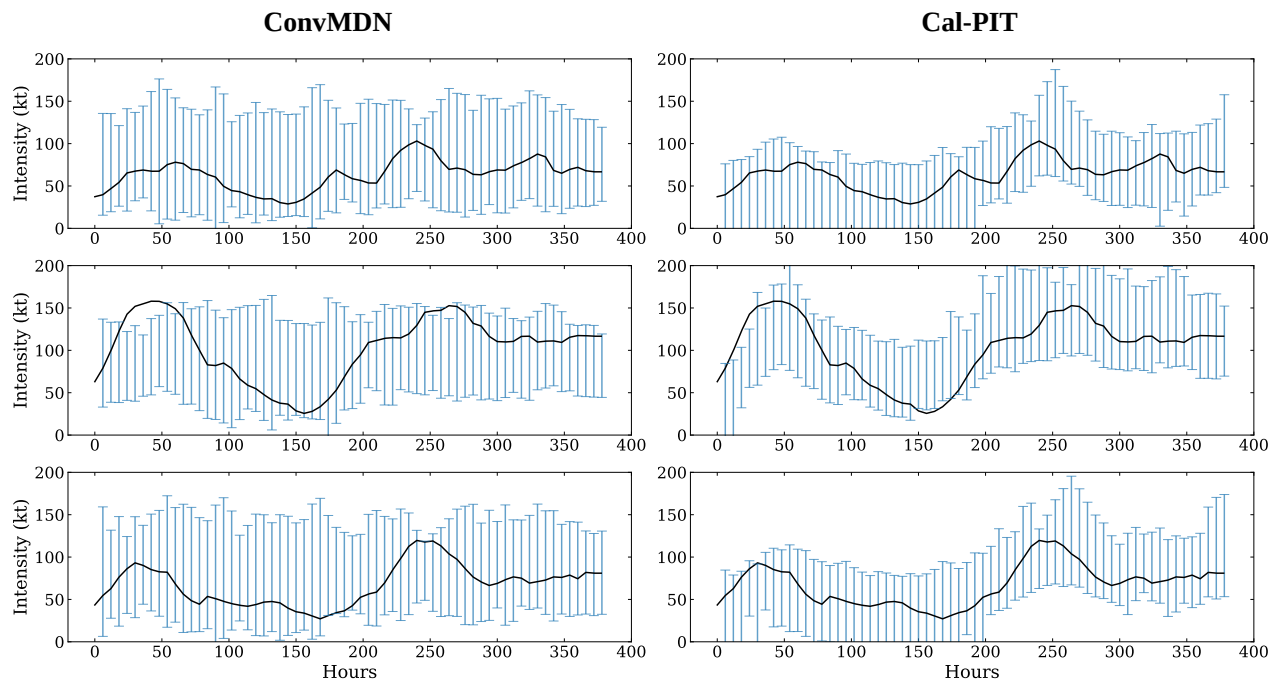


Figure 17: Prediction sets for simulated TCs, before and after calibration. True trajectories are solid black, and prediction sets at test points are in blue.